Journal Pre-proof

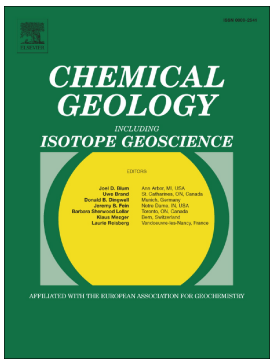

Crystal-chemical variations of spinel, clinopyroxene, and plagioclase in MORB basaltic melt induced by continuous cooling

Letizia Giuliani, Francesco Vetere, Gianluca Iezzi, Manuela Nazzari, Silvio Mollo, Harald Behrens, Piergiorgio Scarlato, Guido Ventura

PII: S0009-2541(22)00059-6

DOI: https://doi.org/10.1016/j.chemgeo.2022.120765

Reference: CHEMGE 120765

To appear in: *Chemical Geology*

Received date: 2 November 2021

Revised date: 25 January 2022

Accepted date: 7 February 2022

Please cite this article as: L. Giuliani, F. Vetere, G. Iezzi, et al., Crystal-chemical variations of spinel, clinopyroxene, and plagioclase in MORB basaltic melt induced by continuous cooling, *Chemical Geology* (2021), https://doi.org/10.1016/j.chemgeo.2022.120765

Crystal-chemical variations of spinel, clinopyroxene, and plagioclase in MORB basaltic melt induced by continuous cooling

Letizia Giuliani[a], Francesco Vetere[a-b], Gianluca Iezzi[a,c], Manuela Nazzari[c], Silvio Mollo[d-c], Harald Behrens[b], Piergiorgio Scarlato[c], Guido Ventura[c,*] fpvetere@gmail.com

[a]Dipartimento di Ingegneria & Geologia (InGeO), Università G. D'Annunzio di Chieti-Pescara, Via dei Vestini 31, 66100, Chieti, Italy;

[b]Institute for Mineralogy, Leibniz University of Hannover, Callinstrasse 3, Hannover, D-30167, Germany

[c]Istituto Nazionale di Geofisica e Vulcanologia, INGV, Via di Vigna Murata 605, 00143, Roma, Italy

[d]Dipartimento di Scienze della Terra, Sapienza Università di Roma, Piazzale A. Moro 5, 00185 Roma, Italy

[*]Corresponding author.

Abstract

In this study we present the compositional changes of clinopyroxene (cpx), plagioclase (plg), spinel (sp), and glass experimentally solidified from an Icelandic MORB melt. The starting material was cooled at P_{atm} and fO_2 of air, in the thermal range of cooling (ΔTc) between 1300 °C (*superliquidus*) to 800 °C (*solidus*) with rates ($\Delta T/\Delta t$) of 1, 7, 60, 180, 1800, and 9000 °C/h. The run products obtained at 1, 7 and 60 °C/h are holocrystalline, whilst between 60 and 180 °C/h plg disappears, and texture of cpx + sp shifts from faceted to dendritic.

As cooling rate increases, we observe that Fe_2O_3 decreases and Al_2O_3 increases in sp and $Al_2O_3 + Fe_2O_3$ increase and CaO + MgO decrease in cpx. These measured variations mirror changes induced by cooling rate in cation (atoms per formula unit, a.p.f.u.) and molecular abundances of these two crystalline phases. Plg composition shows clear linear trends *versus* cooling rate. The chemistry of sp, cpx and, to a minor extent, plg solidified from this basaltic liquid is thus strictly related to the cooling rate condition and is similar to those observed in previous investigations on

alkaline and evolved basaltic systems. In particular, cpx is the only mineral phase profusely present at all the cooling rates, showing the greatest chemical variations in terms of oxides, cations, and components. The intra-crystalline glass (≤ 50 μm from crystal rims) obtained at 180-1800 °C/h shows compositional variations related to the surrounding crystal growth, evidencing strong supersaturation phenomena (such as dendritic texture) due to the establishment of a diffusion-controlled growth regime. Chemical attributes of mineral phases are also quantitatively related with the maximum (G_{max}) and average (G_{CSD}) growth rates of sp, cpx, and plg.

When compared with the starting melt composition, the chemistry of cpx suggests the attainment of near-*equilibrium* crystallization conditions at cooling rate ≤ 60 °C/h, whereas *disequilibrium* effects are found at cooling rate > 60 °C/h. In contrast, plg is in *disequilibrium* with the initial melt chemistry in all experiments. By using thermometric models, the calculated crystallization of plg takes place at temperatures much lower than those of cpx, when the crystal content is high and the diffusion of cations in the melt is slow due to the higher (residual) melt viscosity. Under such conditions and due to the effect of cooling, the system cannot return to homogeneous concentrations and, consequently, plg more effectively records the *disequilibrium* partitioning of cations between the growing crystal surface.

The data-set reported here captures the entire (*superliquidus* to *solidus*) and intrinsic (heterogeneous site-free silicate liquid) solidification behavior from an actual MORB melt from very rapid to extremely sluggish cooling rate. Finally, all analytical relationships found in this work enable careful reconstruction of the solidification conditions of MORB melts, providing novel geo-speedometers for them at high fO_2.

Keywords

MORB, mineral chemistry, solidification kinetics, cooling rate, geospeedometer.

1. Introduction

The chemistry and texture of minerals record the solidification kinetics of silicate melts and are, thus, extremely important to retrieve the crystallization path experienced by volcanic rocks. Cooling rate ($\Delta T/\Delta t$) is one of the most important parameters controlling the solidification of a silicate melt, changing by several orders of magnitude in volcanic systems (Wilding et al., 1995; Vetere et al., 2015; Giuliani et al., 2020a). Mid-Ocean Ridge Basalt (MORB) is the most important and abundant lava type on Earth (Crisp 1984; Gale et al., 2013; Iwamori and Nakamura, 2015), emitted predominantly as nearly dry liquids with $H_2O < 0.1/0.2$ wt.%, (Soule, 2015; Wallace et al., 2015; Zhang et al., 2018) and frequently characterized by aphyric to sub-aphyric textures, containing small amounts of spinel (sp) and abundant clinopyroxene (cpx) and plagioclase (plg) (Coish and Taylor, 1979; Lesher et al., 1999; Zhou et al., 2000).

Solidification experiments are fundamental to understand, constrain, and ultimately quantify the chemical variations induced in minerals by cooling kinetics (Hammer, 2006; Lofgren et al., 2006; Iezzi et al., 2008, 2011; Mollo and Hammer, 2017 and references therein). If these variations are monitored and modelled, then crystal-chemical features in addition to textural features (Giuliani et al., 2020b and c) can depict the crystallization conditions (Putirka, 2008; Zhang, 2008), might inform on cooling regimes undergone by volcanic rocks, and discriminate where and when minerals solidify. Many studies have investigated basaltic systems and have highlighted the possible link between cooling rate and the changes of minerals and host melts (Mevel and Velde, 1976; Coish and Taylor, 1979; Grove and Raudsepp, 1978; Grove and Bence, 1979; Ujike, 1982; Heltz and Thornber 1987; Zhou et al., 2000; Conte et al., 2006; Bagiński et al., 2009; Hammer, 2006; Mollo et al., 2010, 2011a, 2011b, 2012, 2013a, 2013b, 2013c; Iezzi et al., 2014; Mollo and Hammer 2017; Giuliani et al., 2020b and 2020c). It is widely accepted that high cooling rate leads to *disequilibrium*

crystallization conditions (Backer and Grove, 1985; Del Gaudio et al. 2010; Hammer, 2006, 2008; Iezzi et al., 2008, 2011), causing an increase in the concentrations of incompatible elements in a crystal lattice (Lofgren, 2006; Hammer, 2008; Mollo and Hammer, 2017). This is related to the competition between crystal growth and chemical diffusion rates, which favors the enrichment of incompatible cations in the melt feeding the crystal growth (Smith et al., 1955; Smith and Lindsley, 1971; Matsui et al., 1977; Kirkpatrick, 1981; Watson and Liang, 1995; Lasaga, 1998; Wood and Blundy, 1997, Hammer, 2006; Zhang, 2008; Mollo et al., 2010, 2013c) and/or by advection (Kouchi et al. 1986; Vona et al. 2011; Kolzenburg et al. 2018a)

However, only few experimental investigations report on quantitative crystal-chemical modifications induced by cooling kinetics. Among them, the works of Mollo et al., (2010; 2011b; 2013b), Hammer (2006), Baker and Grove, (1985) and in Schiffman and Lofgren, (1982) are useful to be discussed with the aim to show a more comprehensive scenario on the role of kinetics effects in magmatic system. Importantly, these previous studies focus on alkaline, high-Fe or evolved basaltic liquids, whereas actual tholeiitic melt is still not investigated. In particular, sp growing from basaltic melts have been studied by Mollo et al. (2013b). They have illustrated that a $\Delta T/\Delta t$ increase causes a general depletion in $Ti + Fe^{2+}$ coupled with the enrichment of Al + Mg in Etnean trachybasalts. This leads to an increase in spinel *sensu stricto* ($^{T}Mg^{M}Al_2O_4$,) and magnetite ($^{T}Fe^{3+M}Fe^{2+M}Fe^{3+}O_4$) and a decrease in ulvospinel ($^{T}Fe^{2+M}Fe^{2+\ M}Ti^{4+}O_4$) components.

Due to their abundance in basaltic rocks, cpx compositions have been more extensively investigated than sp (Grove and Raudsepp, 1978; Grove and Bence, 1979; Gamble and Taylor, 1980; Mollo et al., 2010, 2013a, 2013c); cpx shows that as cooling rate increases, $^{T}Al + Fe^{3+}$ + Ti+ Na augment, whereas $Si + Fe^{2+}$ + Ca+ Mg deplete. This causes also a general decrease of diopside ($^{M2}Ca^{M1}Mg^{T}Si_2O_6$) + hedenbergite ($^{M2}Ca^{M1}Fe^{2+T}Si_2O_6$) components, and increase of enstatite ($^{M2}Mg^{M1}Mg^{T}Si_2O_6$) + jadeite ($^{M2}Na^{M1}Al^{T}Si_2O_6$) + Tschermak ($^{M2}Ca^{M1}Al^{T}Si^{T}AlO_6$) + CaFe-

Tschermak ($^{M2}Ca^{M1}Fe^{3+T}Si^{T}Fe^{3+}O_6$) components, attesting progressive departure from *equilibrium* crystallization (Mollo et al., 2010; Mollo and Hammer, 2017).

Chemical variations in plg with increasing cooling rate lead to Al + Ca+ Fe^{2+} + Mg enrichments coupled with Si + Na + K depletions. As a consequence, anorthite component ($^{M}Ca^{T}Al_2{}^{T}Si_2O_8$) increases and albite ($^{M}Na^{T}Al^{T}Si_3O_8$) + orthoclase ($^{M}K^{T}Al^{T}Si_3O_8$) components decrease (Mollo et al., 2011b). A similar behavior has been also observed for plg solidified from andesitic and latitic melts (Iezzi et al., 2008; 2011; 2014). The mineral chemistry from solidification experiments is also used to define *equilibrium versus disequilibrium* conditions, as well as to model thermometers, barometers, hygrometers, and geospeedometers (Hammer, 2009; Mollo et al., 2013; Iezzi et al., 2014; Mollo and Hammer, 2017).

Experiments at oxidized (atmosphere fO_2) and reduced (NNO buffer condition) on different eruptive products of Stromboli (evolved basalts) by applying slow (1°C/h) and fast (900 °C/h) cooling rates were investigated to decipher kinetic factors controlling textural and compositional features by Conte et al. (2006). Results indicate that cooling rates have profound implications on crystal size and morphology and growth rate. Polacci et al., (2018) and Arzilli (2019) presented real-time experimental data on crystal nucleation and growth at *disequilibrium* condition, showing the occurrence of crystal nucleation and growth in pulses and point out very fast growth allowing transport properties, such as viscosity, to rapidly increase and possibly cause high energetic eruptions. A similar appraisal is provided by crystallization experiments monitored *in situ* by DSC (Giuliani et al., 2020c). Masotta et al. (2020) also investigate an Etnean basalt at relatively high pressure (4-8 Kbar) in thermal range 1050-1200 °C providing compositional data on clinopyroxenes grown at isothermal conditions and at constant cooling rates. They suggested that hourglass sector zoning could be an effective indicator of sluggish kinetic effects caused by relatively low degrees of undercooling and crystal's growth rate decreases as cooling rate increases. All these studies demonstrate the variability of crystal chemistry with cooling rate.

However, an analysis of the effects of very slow to progressively high cooling rate on the kinetics and chemistry of minerals over a broad thermal range of cooling (ΔTc), i.e. from *liquidus* to *solidus*, has not been investigated yet for actual MORB liquids (Tab. 1). Here, we quantify the compositional changes induced by cooling rate on sp, cpx, and plg solidified from super-*liquidus* conditions at different cooling rates and compare them with the few available experimental literature data, as well as with their textural attributes (Vetere et al., 2013; 2015; Giuliani et al., 2020b). Since the range of applied cooling rate and ΔTc reported in Vetere et al. (2015) and Giuliani et al. (2020b) are the largest ever investigated, the analysis of the mineral chemical changes presented in this study significantly extend previous data and models.

Oxygen fugacity plays major role in magmatic and volcanic systems, although some debate on its correct evaluation in MORB systems still exists (Hammer 2006; Bezòs et al., 2021). Being aware that most MORBs are emplaced at pressure between ~25 MPa at the 2.5 km depth of water and at moderate/reduced fO_2. However, some mid-ocean ridge basalts solidify at pressure of ca. 0.1 MPa and under truly subaerial conditions such as Iceland, and similar spreading tectonic context. (Crisp 1984; Gale et al., 2013; Soule, 2015; Maclennan, 2019). In fact, it is common to find and observe aphyric tholeiitic basalt erupted in several Icelandic places (Óskarsson and Riishuus, 2013 and 2014; Óskarsson et al., 2017). Considering that: 1) cooling-induced solidification experiments were initiated from the super-*liquidus* temperature, 2) they derive from a homogeneous MORB melt and 3) data span for a wide range of temperature (1300-800 °C), our results are relevant for geological condition since aphyric, degassed and oxidized MORBs are abundant. Hence, these data provide general chemical constrains on the crystallization kinetics of the most abundant lavas erupted on Earth.

2. Materials and methods

Chemical analyses were carried out on the run products solidified from dynamic experiments performed by Vetere et al. (2013, 2015). The starting glass material, which has the composition of a natural tholeiitic basalt (B_{100}, Tab. 1), was produced at *P* and fO_2 of air, by cycles of melting at 1600 °C for 4 h, quenching on metal plates and grinding. In particular the starting glass derived from the melting of BIR-1 Standard USGS powdered rocks collected from one of the lava flows often referred to as the Reykjavik dolerites (Flanagan, 1984). ~50 mg of the glass pieces produces were loaded into Pt tubes, squeezed and subsequently welded. The high temperature run was performed in tube furnaces equipped with thermal controllers and at air condition. After quench, duplicated Fe^{2+}/Fe_{tot} was determined by using a modified Wilson method as described in Vetere et al. (2014). BIR-1 standard rock has Fe^{2+}/Fe_{tot} close to 0.8 while in our starting glass Fe^{2+}/Fe_{tot} is 0.4. Experimental literature data derived from starting material used in Mollo et al. (2013a), Hammer (2006), Baker and Grove (1985) and Schiffman and Lofgren (1982) have been added to Tab. 1 for comparison and further discussions.

After experiments, the recovered run products were embedded in epoxy, ground flat, polished, and carbon-coated for microchemical analyses conducted at the HP-HT Laboratory of Experimental Volcanology and Geophysics of the Istituto Nazionale di Geofisica e Vulcanologia in Roma (Italy). Chemical attributes were determined by an electron probe micro-analyzer (EPMA) equipped with five wavelength dispersive spectrometers (WDS). Analyses were performed under vacuum using electron beams of both 2.5 and 5 μm, an accelerating voltage of 15 kV, and an electric current of 7.5 nA. The following standards were used: albite (Na, Si, and Al), forsterite (Mg), orthoclase (K), augite (Fe), rutile (Ti), apatite (Ca and P) and spessartine (Mn). Sodium and potassium were analyzed first, to limit their possible migration. The chemistry of minerals with sizes ≤ 2.5 μm was investigated exploiting the energy dispersive spectrometry (EDS) detector of a field emission gun-scanning electron microscopy (FE-SEM). The operative procedures of FE-SEM and EPMA analyses are extensively illustrated in Iezzi et al. (2008, 2011, 2014) and Vetere et al. (2013, 2015).

Differences in average chemical compositions between EPMA and FE-SEM on 25 analyses conducted on the starting glass are extremely low, as listed in Tab. 1.

Cation (atom per formula unit, a.p.f.u.) and component (mol.%) abundances were computed from measured major oxide elements (wt.%) to satisfy charge balance and typical occupations of crystallographic sites by Si, Ti, Al, Fe, Mg, Ca, and Na in sp, cpx and plg.

3. Results

3.1 Textural features

Starting from the *superliquidus* temperature of 1300 °C (plus one experiment at 1400 °C), the B_{100} melt has been cooled at rate of 1, 7, 60, 180, 1800, and 9000 °C/h, down to 800 °C and rapidly dropping capsules in water (Tab. 2). Run products are characterized by the crystallization of plg, cpx, sp, and glass (Tabs. 3a-d and Figs. 1a-d). Further details on the composition of phases are provided *via* cation (atom per formula unit, a.p.f.u.; supplementary materials Figs. 1S-4S) and component (mol.%) (Figs. 5S-7S) abundances and presented as supplementary material in Tabs. 1S, 2S and 3S. Moreover, we use terms "intra" and "matrix" (Tab. 3d) corresponding to the glass analyzed via EPMA at a distance ≤ and > 50 μm from the crystal rims, respectively.

The complementary textural outcomes of the same run products, in terms of abundance (area%), crystal size distributions (CSD), as well as maximum (G_{max}) and average (G_{CSD}) growth rates, were quantified by Giuliani et al. (2020b) using image analysis on BS-SEM micro-photos (Tab. 4) and are discussed below. Cpx and sp are ubiquitous in the run products, while plg nucleates only at cooling rate ≤ 60 °C/h (< 180 °C/h). The crystal abundances decrease from ca. 100 area% at 1, 7, and 60 °C/h to < 2 area% at 9000 °C/h. Plg content monotonically decreases with cooling rate, while the abundance of cpx increases from 1 to 180 °C/h and then decreases towards 9000 °C/h; sp is always < 5 area% in all run products (Tab. 4). As a general rule, the increase of cooling rate

causes a reduction in crystal size, in concert with the change of crystal shape from faceted to dendritic at $\Delta T/\Delta t \geq 60$ °C/h.

Linear regressions have been built in order to better visualize elements/oxides evolution trends with respect of the applied cooling rate. Only those having coefficient $R^2 \geq 0.8$ for all measured oxides (Figs. 1), cations (Figs. 1S, 2S, 3S and 4S) and components (Figs. 5S, 6S and 7S), have been considered and discussed. For each function found, confidence intervals at the 95% level are reported.

3.2 Variations of oxides

Abundances of major oxides (wt.%) in sp, cpx, plg, and glass are listed in Tab. 3a-d and are plotted in Figs. 1a-d. Also, experimental literature data on synthetic trachybasalt (investigated in Mollo et al. 2010: cpx; 2011b: plg; 2013b: sp), on synthetic Fe-rich basalt (Hammer 2006: sp and cpx), on basaltic andesite (Baker and Grove, 1985: cpx) and on an SiO_2-rich pillow basalt (Schiffman and Lofgren, 1982: cpx and plg) are shown for comparison and further discussion (Tab. 1 and Figs. 1).

For sp, the average amount of TiO_2 is < 1.5 wt.% and it slightly decreases as cooling rate increases. From 1 to 180 °C/h, Al_2O_3 increases by ca. 7 wt.%, while Fe_2O_3 decreases by comparable amount (6.9 wt.%, Tab. 3a). Both TiO_2 and Fe_2O_3 trends follow a linear relationship with cooling rate and a slight decrease at higher $\Delta T/\Delta t$ (Fig. 1a). A more complex trend is observed for MgO, showing a slight decrease by ca. 4 wt.% between 7 and 60 °C/h and then an abrupt increase by ca. 5 wt.% up to 180 °C/h (Tab. 3a, 1S and Fig. 1a). Model predictions computed by using alphamelts 1.9, at the experimental fO_2 close to QFM + 2.5 (QFM: quartz-fayalite-magnetite buffer; Asimow and Ghiorso 1998; Ghiorso et al., 2002; Smith & Asimow, 2005), results sp in at temperature of 1084 °C ($Fe^{2+}_{1.23}Mg_{0.29}Fe^{3+}_{0.78}Al_{0.17}Cr_{0.00}Ti_{0.52}O_4$). Indeed, even at 1°C/h the dynamic cooling experiments solidify sp richer in Fe and more depleted in Ti with respect of the theoretical

equilibrium conditions (Fig. 1a). At the highest cooling rates, experimental spinel composition deviates even more from those predicted by alphaMELTS.

For cpx, only CaO show a linear and well-defined trend as a function of cooling rate (Fig. 1b), although its variation shows a significant decrease only between 180 and 1800 °C/h, while: i) SiO_2 slight decreases from 1 to 180 °C/h and then remains almost constant up to 1800 °C/h, ii) Al_2O_3 increases by ca. 8 wt.% from 1 to 1800 °C/h, iii) MgO decreases by ca. 4 wt.% and iv) Fe_2O_3 shows a slight increase at higher cooling rates (Tab. 3b and Fig. 1b). This could possibly reside to the fact that more acicular habits and tiny sizes (as those obtained at 1800 °C/h) will result in entrapment of interstitial melt, which 1) could affect the element mobility and 2) add relative difficulties in the analytical measurements of narrow melt pools (Giuliani et al., 2020b). In this case, alphaMELTS prediction results in good agreement with our data at lowest cooling rate except for Fe and Mg. These discrepancies derive from the computed assemblage modelled that fractionate olivine and 2 cpx; cpx1 virtually appears at 1192 °C and evolve in composition from $Na_{0.01}Ca_{0.79}Fe^{2+}_{0.16}Mg_{0.93}Fe^{3+}_{0.04}Ti_{0.01}Al_{0.17}Si_{1.89}O_6$ to $Na_{0.02}Ca_{0.79}Fe^{2+}_{0.28}Mg_{0.78}Fe^{3+}_{0.05}Ti_{0.03}Al_{0.19}Si_{1.86}O_6$ as temperature drop down to 992 °C. Cpx2 appears at 1149 °C and evolve in composition from $Na_{0.01}Ca_{0.28}Fe^{2+}_{0.42}Mg_{1.21}Fe^{3+}_{0.03}Ti_{0.00}Al_{0.13}Si_{1.92}O_6$ to $Na_{0.00}Ca_{0.19}Fe^{2+}_{0.60}Mg_{0.78}Fe^{3+}_{0.05}Ti_{0.03}Al_{0.01}Si_{1.92}O_6$ as temperature drop down to 992 °C. In Fig. 1b only composition at the lowest temperature (close to $T_{solidus}$) are reported.

All the major oxides of plg, except Na_2O, show very little change and follow almost linear trends with high regressions (Fig. 1c). All the oxides vary faintly between 1 and 7 °C/h, while as the cooling rate increases up to 60 °C/h, SiO_2, Fe_2O_3 and Mg also increase, and Al_2O_3 and CaO decrease (Tab. 3c and Fig. 1c). Alphamelts *equilibrium* condition data reported in Fig. 1c show putative feldspar composition evolving from high Ca and Al contents at high temperature (1217 °C) as first phase on *liquidus* ($K_{0.00}Na_{0.17}Ca_{0.83}Al_{1.83}Si_{2.17}$) to high Na and low Al content at 1042 °C ($K_{0.03}Na_{0.66}Ca_{0.31}Al_{1.31}Si_{2.69}$)

Intracrystalline glass is found in runs at 180 and 1800 °C/h. SiO_2 decreases by ca. 4 wt.% as cooling rate increases, and Fe_2O_3 increase by ca. 3 wt.%, whereas variations in Al_2O_3, MgO, CaO, and Na_2O contents are within the analytical uncertainty (Tab. 3d). The matrix glass is observed only at cooling rates ≥ 1800 °C/h, and its composition is almost homogeneous with variations ≤ 1 wt.% (Fig. 1d).

3.3 Variations of cations

Cation abundances (a.p.f.u.) are calculated considering 3, 4, and 5 cations and 4, 6 and 8 oxygens for sp, cpx, and plg, respectively. As expected, cation variations generally reflect the wt.% trends as a function of cooling rate (Figs. 1S, 2S, 3S and 4S), showing standard deviations always ≤ 0.1 a.p.f.u. for all the mineral phases (Tabs. 1S, 2S and 3S).

On average, the amount of Ti changes little but show a definite linear decreasing trend, while Mg in sp remain almost constant; from 1 to 60 °C/h, Al increases by 0.3 a.p.f.u.. Fe^{3+} decreases by 0.3 a.p.f.u. and Fe^{2+} increases by 0.2 a.p.f.u. (Tab. 1S). Resulting from these trends, Fe^{tot} is almost constant between 1 and 60 °C/h and then decreases up to 180 °C/h, while Fe^{2+}/Fe^{tot} increases from 7 to 60 °C/h and decreases up to 180 °C/h (Fig. 1S). Only Fe^{tot} shows a constant trend for the 3 lowest cooling rates, but it decreases for the highest cooling rate.

The variations of cations in cpx are reported and shown in Tab. 2S and Fig. 2S, 3S. Si and ^{T}Al show limited and also scattered variations as cooling rate increases, whereas ^{M1}Al increases by 0.3 a.p.f.u from 1 to 1800 °C/h. Al^{tot} mirrors the same trend of ^{M1}Al. Fe^{2+} and Fe^{3+} show slight increasing and decreasing trends, respectively, resulting in an almost constant trend of Fe^{tot} as a function of cooling rate. Thus, this could reflect the ability of melt to re-equilibrate albeit the imposed fO_2 is the same. For instance, fast cooling will result in the melt "remembering" the lower fO_2 at the high T equilibration (Fig. 3S), whereas fO_2 can equilibrate quite efficiently for slow cooling rates and small samples. Similarly, Mg and Ca stay more or less constant from 1 to 180

°C/h and then decrease from 180 to 1800 °C/h. Na is invariably ≤ 0.1 a.p.f.u. showing an no systematic trend. Note that only Ca is linearly and robustly correlated with cooling rate. Particularly, as $\Delta T/\Delta t$ increases Fe^{2+}/Fe^{tot} increases by at least the 20%, whereas Mg# decreases from 93 ± 4 to 72 ± 7 (Fig. 3S and Tab. 2S).

Plg records weak average variations of cations; the increasing of Si is the most significant ones, contrarily to those of Fe^{3+}, Al and Ca (Fig. 4S). Mg is ≤ 0.01 a.p.f.u. in all the experimental charges and, for this reason, it is not considered in Tab. 3S and Fig. 4S.

3.4 Variations of molecules

Sp is a solid solution of the magnetite (Mag), spinel *sensu stricto* (Sp *s.s.*), and ulvospinel (Usp) end-members. Mag is the most abundant component, although Sp *s.s.* amount became relevant at higher cooling rates. The increasing of the latter follows linear functions as the cooling rate increases (Fig. 5S). Usp content is ≤ 10 mol.% on average, weakly increasing from 1 to 60 °C/h and then decreasing up to 180 °C/h (Tab. 3S and Fig. 5S).

Cpx is expressed in terms of diopside (Di), hedenbergite (Hd), enstatite (En), ferrosilite (Fs), Tschermak (Ts), CaFe-Tschermak (CaFeTs), CaTi-Tschermak (CaTiTs), and jadeite (Jd) components (Tab. 2S and Fig. 6S). From 1 to 60 °C/h, cpx mainly consists of Di > 40 mol.%, plus En + Ts of about 20 and 12 mol.% on average, then the amount of Di is almost halved and that of Ts increases (Fig. 6S). As for the sp and plg, also the cpx components show limited variations from 1 to 60 °C/h, while between 60 and 1800 °C/h, Di and CaFeTs decrease, En + Fs + Ts slightly increase, and Hd, Jd and CaTiTs do not display relevant variations (Tab. 2S and Fig. 6S). Between all the cpx components, only the increasing of Fs linearly scales with cooling rate (Fig. 6S).

Plg is expressed in terms of anorthite (An) and albite (Ab), since the amount of orthoclase is negligible. However, as cooling rate increases, both An and Ab are almost constant, basically

reflecting their small cation changes (Fig. 7S). Even if very low, An-variations align along linear functions (Fig. 7S).

3.5 Classification and abundance of minerals

In the Mag - Sp *s.s.* - Usp ternary diagram, the composition of sp (Fig. 8S) mainly falls along the Mag - Sp. s.s. solid solution field, with only a limited amount of Usp, which is always ≤ 10 mol.% (Fig. 8S). According to the quadrilateral of Morimoto (1988), cpx is classified as augite (Figs. 8S and 3). In the Ab-An-Or ternary diagram plg is mostly labradorite and minor bytownite (Fig. 8S).

The abundance of crystals and glass determined by image analysis (Giuliani et al., 2020b) are here compared with those from least-square mass balance calculations based on the average chemical composition of phases (Fig. 9S). The retrieved area% and wt.% generally agree, although some discrepancies are evident especially for plg and cpx solidified at 1 and 7 °C/h, where the estimates are different (Fig. 9S and Tab. 3). Plg varies from 65.6 to 60.7 (area%) and 42.5 to 40.5 (wt%) while cpx varies from 30.6 (area%) to 36.0 (area%) and 51.2 and 55.2 (wt%), respectively, when cooling rate is from 1 to 7 °C/h. The resulting mass balance underestimates the plg crystal content systematically by ca. 20% and overestimate cpx by ca. 20%. This can be attributed to the variations (core to rim) of chemical compositions of these crystalline phases, especially at slow cooling rates, when the crystal content is extremely high. As an example, in agreements with literature data based on cooling experiments on Etna basalt (Mollo et al., 2011), we do observe core to rim (En54 *vs* En43, respectively) compositional variation in cpx at 1 °C/h. This result is however not ubiquitous since there are crystals showing some scatter in the chemistry due to the dynamic systems imposed.

4. Discussion

A first important result from this study is that increasing the cooling rate, most of the wt.% of major oxides in minerals gradually approach that of the starting bulk composition (Figs. 1). This especially holds for Al_2O_3 and TiO_2 in sp (Fig. 1a), Al_2O_3, Fe_2O_3, MgO and CaO in cpx (Fig. 1b), and for Al_2O_3, Fe_2O_3, MgO and CaO in plg (Fig. 1c), suggesting the *disequlibrium* incorporation in the mineral lattice site of especially sluggishly diffusing Si, Ti, and Al high field strength elements. Instead, the SiO_2 contents of plg differ from the starting bulk amount (Fig. 1c); however, this is probably related to the SiO_2 enrichment in the residual melt(s) from whom it crystallizes after sp and cpx (see below). This behavior can be related to the fact that the melt is more rapidly cooled from *liquidus* to the *solidus* temperatures, preventing significant mobility of cations, especially the less mobile like Si, from the initial atomic distribution inherited from super-*liquidus* conditions. This diffusion behavior is qualitatively in line with previous observations conducted in experiments (Kirckpatrick, 1981; Dunbar et al., 1995; Roskosz et al., 2005, 2006; Iezzi et al., 2008, 2009, 2011; Del Gaudio et al., 2010; Mollo et al. 2010, 2011b, 2013; Vetere et al., 2013, 2015) and for naturally cooled volcanic rocks (Coish and Taylor, 1979; Gamble and Taylor, 1980; Lesher et al., 1999; Dingwell, 2006; Villeneuve et al., 2008, Gnistyakova and Latypov, 2009), and should couple with advection process acting as counterbalance in diffusion constrained crystal growth and reducing the intensity of the disequilibrium as shown by Kouchi (1986), Vona (2011) and Kolzenburg (2018).

Cpx is the only mineral phase that is present in significant amount at all the cooling rates, and the one showing the greatest chemical variations in terms of oxides, cations, and components (Tabs. 3b, 2S and 4 and Figs. 1b, 2S and 6S). Considering the fO_2 experimental conditions, chemical variation in cpx has the potential to retrieve the thermal paths of the MORB liquids or in general basaltic systems and could be employed to model the kinetics of cooling for these rocks (see below). The available experimental literature data on starting composition presented in Tab. 1 and those computed by using alphamelts 1.9 (Asimow and Ghiorso 1998; Ghiorso et al., 2002; Smith & Asimow, 2005) are also reported in Figs. 1a-d.

4.1 Cation exchanges in cpx

Fig. 2 shows the variation of Fe^{3+}, ^{M1}Al, and Fe^{2+} in cpx *versus* the other major cations as a function of cooling rate. The increase of Fe^{3+} is linearly correlated with the decrease of Fe^{2+} and ^{M1}Al (R^2 = 0.87-0.89). In a similar fashion, the increase of ^{M1}Al is linearly related with the increasing of $Fe^{2+}$and to the decreasing of Fe^{3+} + Mg (R^2 = 0.82-0.97), while the increase of Fe^{2+} determines a linear decreasing of Fe^{3+} and Ca and an increasing of ^{M1}Al (R^2 = 0.89-0.97) (Fig. 2). In turn, such relationships are the most valuable to retrieve kinetics of solidifications of MORB melts.

The high linear correlation between Fe^{3+} and ^{M1}Al (Fig. 2) is dictated by the substitution of these two cations in the same M1 site (Deer et al., 1997; Mollo et al., 2013c), leading to a decrease of CaFeTs coupled with the increase of CaTs as the cooling rate increases (Fig. 6S). The increase of Hd and the decrease of CaFeTs (Fig. 6S) highlight the effect of cooling kinetics on the coupled substitutions Fe^{3+} + ^{T}Al for Fe^{2+} + Si, and the consequent collinearity between Fe^{3+} and Fe^{2+} (Fig. 2). Likewise, the decrease of Di coupled with the increase of Hd + Fs (Fig. 6S) indicates that Fe^{2+} is replaced by both Ca and Mg as cooling rate increases (Fig. 2). Fig. 2 also shows that cation exchanges operate at the same M1 crystallographic site of cpx (i.e., Fe^{3+}*versus*^{M1}Al and Fe^{3+}*versus* Fe^{2+}), at the M2 site (i.e., Fe^{2+} *versus* Ca), as well as both M1 and M2 sites (^{M1}Al *versus* Fe^{2+}, and Fe^{2+}*versus*^{M1}Al).

According to these cation exchanges, there is collinearity between the most abundant (> 10 mol.%) components in cpx (i.e., Di *versus* En + CaTs, Figs. 3). Moreover, the ratios between these components (i.e. Di/(En+CaTs)) scale with the cooling rate following a logarithmic function (Figs. 3). This condition of linear and logarithmic functions implies that the compositional changes of cpx can be used as a proxy for solidifying MORB systems over either very rapid or extremely slow cooling rates. Therefore, the relationships provided in Figs. 2 and 3 are geospeedometers.

4.2 Mineral chemistry versus textures

Several experimental studies focusing on melt crystallization kinetics lack for an overall discussion in which the changes in chemical and textural parameters of minerals are concurrently quantified and evaluated (Coish and Taylor, 1979; Gamble and Taylor, 1980; Tsuchiyama, 1985; Dunbar et al., 1995; Lesher et al., 1999; Couch, 2003; Hammer, 2006, 2008; Pichavant et al., 2007; Iezzi et al., 2008; Pupier et al., 2008; Schiavi et al., 2009; Mollo and Hammer, 2017). This gap can be here addressed by comparing the textural analysis conducted by Giuliani et al., 2020b with chemical data presented in Figs. 1, 2, 3 and 1S, 2S, 3S, 4S, 5S, 6S plus 7S as a function of cooling rate. Particularly, in this context, we refer to G_{max} and G_{CSD} (Tab. 4), that result linearly correlated with a $R^2 \geq 0.80$ with some oxides (wt.%.) and components (mol.%) of sp, cpx and plg (Figs. 4).

As reported in Giuliani et al., (2020b), the maximum growth rate is calculated by averaging the major axes (L_{max}) of the five longest crystals and dividing them by the cooling time ($G_{max} = L_{max}/t$). The average growth is calculated by interpolating the CSD slope (m) and the cooling time (t), as $G_{CSD} = -1/mt$. For sp, G_{max} and G_{CSD} follow linear trends when compared with Sp *s.s.* (Fig. 4a), while only G_{max} is linearly related with Fe_2O_3. For cpx, G_{max} follows linear trends with CaO and Di, Fs and CaFeTs, while G_{CSD} is related with Fe_2O_3, Hd and Jd (Fig. 4b and 4c). For plg, G_{max} is successfully linearly regressed *versus* Fe_2O_3, An and Ab, whilst G_{CSD} correlates only with Na_2O (Fig. 4d). All these analytical functions agree with the fact that the incompatible cations are preferentially incorporated from the melt into the lattice site of the rapidly growing crystal (Mollo and Hammer, 2017). In other words, the *disequilibrium* mineral composition is sympathetic to the enrichment/depletion of cations as a function of time averaged growth rate. The decrease in crystal size and increase of time averaged growth rates with increasing cooling rate (Kolzenburg et al., 2020; Giuliani et al., 2020b, Tab. 4 and Figs. 4) is proportional to these supersaturation phenomena and the lack of melt re-homogenization; in turn, well-faceted crystal morphologies change into dendritic branches more enriched in incompatible and slow diffusing cations, such as Al and Fe^{3+} (Figs. 4), in the melt (Pontesilli et al., 2019).

The obtained good regression statistics ($R^2 \geq 0.81$-0.99) between mineral compositions and *G*s allow us to derive the crystal growth rate from simple chemical analyses of sp, cpx, and plg in a solidifying MORB system. (Figs. 4a, 4b and 4c).

4.3 Crystallization of sp, cpx, and plg from basaltic melts.

The oxide compositional variations observed in this study (Figs. 1) are compared with those reported for an Etnean trachybasaltic (Mollo et al., 2010; 2011b, 2013b), a synthetic Fe-rich basalt (Hammer, 2006), a basaltic andesite (Baker and Grove, 1985) and an SiO_2-rich pillow basalt (Schiffman and Lofgren, 1982) melts (Figs. 1 and Tab. 1). The starting composition B_{100} used here is very close to that of Mollo et al. (2013a) except for MgO, Na_2O and K_2O, whereas the starting composition reported in Hammer (2006) is significantly richer in FeO, slightly lower in SiO_2 and markedly poorer in Al_2O_3 and more depleted in MgO and CaO (Figs. 1 and Tab. 1). Compared to our bulk MORB system those experimented by Baker and Grove (1985) and Schiffman and Lofgren (1982) are both richer in SiO_2 plus alkalis and both poorer in MgO plus CaO; the former study used a relative Al_2O_3-rich and FeO-poor melt, the latter a relative Al_2O_3-poor and FeO-rich melt (Figs. 1 and Tab. 1). Therefore, the bulk chemical differences shown in Figs. 1 provide a general appraisal of dynamic solidification induced by cooling at P_{atm} and variable fO_2.

Mollo et al (2010; 2011b and 2013b) alkaline basaltic melt undergo solidification in laboratory at fO_2 of 1.5 log units above the nickel-nickel-oxide buffer (NNO+1.5) equivalent to QFM+2.2 (recalculated here, with QFM: quartz-fayalite-magnetite buffer). The experimental cooling rate were 30, 126, 180, 564, at temperature of 900 °C/h. Cooling rates were initiated at 1250, 30 °C above the $T_{liquidus}$ of 1220 °C, and terminated at 1100 °C, significantly above the *solidus* (Del Gaudio et al., 2010; Mollo et al., 2010, 2011b and 2013c). Hammer (2006) experiments were

run at fO_2 from QFM-4 to QFM+5, cooling rates of 2.8, 5.7, 18.7, 72.4, and 231 °C/h, started from a T of 1210 °C, close to the estimated $T_{liquidus}$ ranging between 1205 and 1245 °C (as a function of fO_2); the quenching was done at temperature between 300-400 °C, far below the *solidus*. Experiments performed by Baker and Grove (1985) were run at fO_2 of QFM buffer at cooling rate of 50, 10, 5, 1 and 0.5 °C/h; however, only the 0.5, 1 and 5 °C/h experiments reported chemical analyses of phases. Initial experimental temperature was set at 1170 °C, 20 °C below the reported $T_{liquidus}$ and contained already plg and ol at the initiation of cooling; they terminated the cooling rates between 1108-1055 °C above the *solidus*. Finally, experiments presented by Schiffman and Lofgren (1982) were also run at QFM buffer, using cooling rates of 0.5, 1, 10, 25, 84, 120 and 218 °C/h, respectively. The *liquidus* temperature was estimated to be 1140 °C (presumably too low for this system) and the cooling rate initiated at 1125 °C, so in the presence of already formed crystals; the experimental runs were quenched close to 1000 °C, thus before the *solidus* temperature.

Thereby, only our B_{100} melt and that used by Mollo et al. (2010; 2011b and 2013b) initiated the solidification well above the *liquidus*, while Hammer (2006), Baker and Grove (1985) and Schiffman and Lofgren (1982) started close or even below *liquidus* temperatures. Consequently, the latter three investigations could nucleate heterogeneously on early-formed crystalline phases (Vetere et al., 2013 and 2015) and from already evolved melts before the onset of their applied dynamic cooling conditions. In parallel, only our experiments and those of Hammer (2006) terminated at or below *solidus* region, constraining the entire crystallization sequence. Our run-products are the only ones performed at very high fO_2 environment, i.e. air (see below), where the other change from very reduced to relative oxidized conditions (Figs. 1). To summarize, only the data-set reported here captures the entire (*superliquidus* to *solidus*) and intrinsic (heterogeneous site-free silicate liquid) solidification behavior from an actual MORB melt from very rapid to extremely sluggish cooling rate. In sp, the increase of $\Delta T/\Delta t$ induces a pronounced decrease of TiO_2 in the trachybasalt (Mollo et al., 2013b), while in our tholeiitic B_{100} and Fe-rich basalt of Hammer

(2006) such behavior is more restricted (Fig. 1a). The Fe_2O_3 in Mollo et al. (2013b) and Hammer (2006) follow similar slightly variable trends, while in the B_{100} the sp is progressively depleted especially at high cooling rate; in parallel, the Fe_2O_3 contents from the trachybasalt and Fe-rich liquids are higher than in the B_{100}, although the latter was solidified at the highest redox condition (Fig. 1a). The amount of Al_2O_3 in sp increases either in the B_{100} and trachybasalt systems, but is slightly variable in the Fe-rich basaltic liquid. The amount of MgO follows a scattered behavior for the B_{100} and Fe-rich basaltic liquids and increasing for the trachybasalt (Fig. 1a, 1S). On the whole, these trends can be explained by the slower diffusion of the high field strength Ti with respect to Al and Fe^{3+}, favoring the increasing of the spinel s.s. molecule when cooling rate increases (Fig. 5S) (O'Donovan and O'Reilly 1977; Kirkpatrick, 1983; Pick and Tauxe, 1994; Hammer, 2006; Lofgren, 2006; Mollo et al, 2010, 2013b; Chadima et al. 2009).

In natural domains, MORB-pillows, lava flows and dikes show that Ti content in sp changes as a function of cooling rate, i.e. moving from the inner to the outermost portions and chilled margins (Smith and Prévot 1977; Zhou et al. 2000; Kissell et al. 2010; Mollo et al. 2011a, 2013b). Since the trends of TiO_2, Al_2O_3, Fe_2O_3 and MgO are only crudely similar from the three basaltic liquids compared in Fig. 1a, it can be concluded that the effect of cooling rate on sp is extremely sensitive to the melt bulk composition. Interestingly, the trends of Fe_2O_3, Al_2O_3 and MgO displayed in Hammer (2006) for sp are weakly affected by strong variations in fO_2, whereas TiO_2 is more straightforward affected, at least at low cooling regimes (Fig. 1a).

For cpx, chemical trends for both B_{100} and Etnean trachybasalt studied by Mollo et al., (2010), show again several similarities (Fig. 1b), at least in the range of $\Delta T/\Delta t$ = 30-900 °C/h. The increase of cooling rate causes a very similar increase of both Al_2O_3 and Fe_2O_3 and a slight decrease of both CaO and MgO (Fig. 1b). The SiO_2 content of the trachybasalt decreases monotonically, whereas it is less regular for B_{100} (Fig. 1b). These relationships indicate that cpx behaves in a very similar way in B_{100} and trachybasalt despite their differences in bulk chemical composition and imposed fO_2

conditions. Again, cpx is more appropriate for the calibration of general models based on a large experimental data set and due to their larger crystal sizes with respect to sp (Tab. 4), cpx can be easily analyzed also at high cooling rate.

The chemical features of cpx as a function of cooling rate constrained in Hammer (2006) are in general more significantly scattered with respect to those provided here and by Mollo et al. (2010). However, the increasing trends displayed in Hammer (2006) by both Fe_2O_3 and Al_2O_3, mainly at the highest fO_2, are similar to those observed here and by Mollo et al. (2010). SiO_2 and MgO show similar behavior and a decreasing concentration at higher cooling rate (Fig. 1b). At low rates, the evolved basaltic melt of Schiffman and Lofgren (1982) show decreasing for SiO_2 and increasing for Al_2O_3 trends similar to our outcomes when cooling rate increases, whereas the other oxides are extremely scattered (Fig. 1b). Finally, the basaltic andesite system investigated in Baker and Groove (1985) has composition of cpx that are close to those measured for B_{100} at the lowest cooling rate (Fig. 1b). To sum up, Al_2O_3 is the most sensible oxide component to cooling rate in cpx grown in basaltic rocks from tholeiitic to basaltic andesite systems, as well as in Fe-rich systems (Fig. 1b).

For plg, chemical data of B_{100} differ significantly with respect the trachybasalt (Mollo et al., 2011a) and the evolved basalt (Schiffman and Lofgren, 1982) like shown in Fig. 1c. In these latter two studies SiO_2 decreases whilst in B_{100} broadly increase when $\Delta T/\Delta t$ augments; the other oxide components in B_{100} follow well defined trend, but their actual variations are extremely limited and in general opposite to those displayed from run-products in the trachybasalt and evolved basalt. The qualitative trends are instead similar for the incompatible and minor Fe_2O_3 and MgO (Fig. 1c). Importantly, the two previous studies on plg were quenched at high T, compared to the 800 °C used for B_{100}. This implies that the run-products of these previous studies (Mollo et al., 2011b; Schiffman and Lofgren, 1982) were quenched in the presence of a residual liquid, i.e. the solidification paths were halted before the possible occurrence of further crystallization.

Consequently, the different trajectories observed for the compatible cations are ascribed to the different thermal ranges of the experiments at low-*T*, bearing in mind that plg is the last mineral phase that crystallizes from the B_{100} melt (see below). In agreement, the trachybasalt was invariably glass-bearing (> 20 area%; Mollo et al., 2011b), while B_{100} was always holocrystalline at cooling rate ≤ 60 °C/h (Tab. 4). As a consequence, compatible cations in the trachybasalt are partitioned between crystal and glass. In contrast, compatible and incompatible cations in the B_{100} are invariably incorporated in the lately grown framework-silicate mineral. It remains the fact that incompatible cations can be potentially used as a proxy for cooling rate, due to their sensitivity to the formation of a diffusive boundary layer in the melt supplying nutrients at *disequilibrium* proportions to the rapidly growing plg crystals (Mollo et al., 2011b).

On the whole, all data in Figs. 1 display a relative wide variation *versus* cooling rate. The first reason resides to kinetics effect. In fact, chemical difference on the residual melts (Fig. 1d) result in different proportion of the growing ingredient for crystals (Figs. 1a, b and c), up to a factor of ca. 10x (e.g., TiO_2 in sp from H2006 data Fig. 1a). The second aspect to be considered are due to differences in core to rim compositions, especially at low cooling rates. This is expected during crystal growth as the phases tend to continuously approach *equilibrium*, here represented by virtual sp, cpx and plg phases computed by alphamelts on the B_{100} basaltic system at *solidus* temperature of 800 °C (Figs. 1).

4.4 The role of fO_2 in basaltic melts undergoing solidifications

Since the 1950s it was acknowledged the importance of fO_2 and its role in igneous differentiation (Kennedy, 1955; Eugster, 1957; 1959; Osborn, 1959) and tectonic settings (Haggerty, 1976; Christie et al., 1986; Wood et al., 1990; Carmichael, 1991; Frost and Lindsley, 1992; Ballhaus, 1993; Canil, 1997). Calc-alkaline magmatic series crystallize under relatively high fO_2 and at convergent plate boundaries, while tholeiitic magma series experienced low fO_2 mainly

at divergent boundaries (Fig. 5a). However, Rowe et al., (2009) re-determined the fO_2 in melt inclusion hosted in olivine from primitive basaltic lavas sampled from across the central Oregon Cascades to a more oxidized range of -0.25 < QFM < + 1.9. All these data highlight that MORBs can be also emplaced in relatively oxidized environments over the Earth crust, either in subaerial or submarine domains (Crisp 1984; Gale et al., 2013; Soule, 2015). In parallel; magmas *en route* to the Earth surface commonly slightly oxidized (Burgisser and Scaillet, 2007). In summary, data derived from literature indicate that MORBs lie around QFM buffer reaching sometimes value close to QFM+1, while other basaltic melts in different geological context can be even more oxidized (Cottrell et al., 2020; Fig. 5a).

In addition to this general reappraisal, it is relevant to consider several other aspects on the relationship between fO_2 and Fe-bearing crystalline phases solidified from basaltic melts either in nature and experimental charges, such as: i) close or open system conditions, ii) kinetics of re-equilibration during the solidification at variable temperature and iii) crystal-chemistry constraints on the arrangement of Fe^{2+} and Fe^{3+} in crystalline structures (Iezzi et al., 2005; Della Ventura et al., 2006). All these aspects are relevant for the interpretation of our and literature experimental data (Figs.1, 1S-8S and 2), plus the following possible critical aspects. The redox state is not always accurately quantified in many of the experiments from literature and a lot of runs were simply buffered to the intrinsic oxygen fugacity (fO_2) of the experimental capsule. If $aH_2O < 1$ under self-buffered conditions, an apparent redox state is attained within the capsule by the relationship: log fO_2 capsule = fO_2 apparent + $2\ln(aH_2O)$ (Vetere et al., 2014). Additionally, the gas phase in the capsule typically contains an uncontrolled amount of X_{N2}^{fluid} due to incorporation of atmospheric nitrogen during loading of the powder into the capsule. This may represent a further source of error (Behrens et al., 2009). Finally, charge-balance equations are affected by a large degree of uncertainty and such calculations do not guarantee that the Fe^{2+} and Fe^{3+} contents are correctly quantified, due to intrinsic uncertainties obtained by using EPMA rather than Mössbauer or other

spectroscopic methods (Putirka et al., 2003; McGuire et al., 1989; Di Genova et al., 2016 and 2018). In line, modelling clinopyroxene components and *equilibria* as a function of *P*-*T*-H_2O conditions relies on the measurement of FeO^{tot} rather than the calculation of Fe^{2+}/Fe^{3+} ratio in clinopyroxene (Putirka, 2008 and references therein). Therefore, great caution must be exercised in the assessment of the relationship between clinopyroxene-melt components and fO_2, when only EPMA data are available.

The B_{100} homogeneous starting glass has Fe^{2+}/Fe^{tot} close to 0.4 after been rapidly quenched from 1300°C subsequent to a dwell of at least 2 h (Tab. 1). In fact, as reported in Vetere et al., (2013), the low viscosity of basaltic composition at 1300°C (ca. 20 Pa s) allows fast re-equilibration and relatively high diffusivity, close to ln(D) = -24.5. If it is considered $x = (2Dt)^{0.5}$ as minimum homogenization distance in a melt with time (t), then it can be calculated a distance close to 0.2 mm in 2 h, for sluggish diffusive elements such as Si, Al and Fe^{3+}. This time is enough to allow melt relaxation and equilibration (Vetere et al., 2013).

According to the model of Kress and Carmichael (1991), an Fe^{2+}/Fe_{tot} of 0.4 (Tab. 1) corresponds to a hypothetical redox state intermediate between 2.5 < QFM < 3 for temperatures ranging from T_m (1206 °C as measured in Giuliani et al., 2020c) and 1300 °C of the B_{100}, thus significantly lower than the redox state corresponding to that of air (Fig. 5b). Interestingly, the high-Fe basaltic melt investigated by Hammer (2006) indicates that even a huge variation in fO_2 determines a relative low variation in the amount of Fe_2O_3 in sp, that is close to that observed in the B_{100} melt, especially at QFM+5 (Fig. 1a), although it affects the *T* at which it crystallizes. An even more similar behavior is shown by the trends of iron (total iron calculated as Fe_2O_3) of the cpx in the B_{100} in comparison with the high-Fe basaltic melt of Hammer (2006) and the trachybasalt of Mollo et al. (2010) (Fig. 1b). The amount of Fe_2O_3 in plg, albeit very low, is similar between B_{100} and the evolved basaltic system of Shifman and Lofgren (1982) (Fig. 1c). All these similarities attest that our results are close to those obtained at QFM and higher fugacity conditions. We

speculate that such behaviors of Fe in sp, cpx and plg *versus* fO_2 in solidifying basaltic melts can result from internally buffered conditions in capsules and on short range arrangement of Fe^{2+} and Fe^{3+} in the crystallographic sites of these crystalline structures.

4.5 Equilibrium versus disequilibrium crystallization

Mollo and Hammer (2017) have reviewed how rapid crystal growth conditions caused by increasing cooling rate lead to the *disequilibrium* uptake of incompatible elements in mineral-bearing basalts with respect to *equilibrium* cation partitioning. On the whole, *disequilibrium* crystallization at 250-350 °C above the *solidus* region produces enrichments of Mag, Ts + Jd + En + Fs, and An that are accompanied by depletion of Usp, Di + Hd, and Ab + Or in sp, cpx, and plg, respectively.

In this study, we observe that Sp s.s. increases, Mag decreases with $\Delta T/\Delta t$, whereas Usp first increases in faceted sp crystals obtained at 1-60 °C/h and then decreases in dendritic crystals forming at higher cooling rate (Fig. 5S). A more complex compositional change of sp is observed for MORB melts undercooled within the *solidus* region but, in general, the effect of kinetics is better recorded by the *disequilibrium* partitioning of Al that is systematically incorporated in the lattice site when the cooling rate increases (Fig. 2a).

For cpx, the enrichment in Al with cooling rate is also an indication of progressive departure from *equilibrium* (Mollo et al., 2010; Mollo and Hammer, 2017). Considering the limits of the standard errors, from 1 to 7 °C/h, Al does not substantially change in cpx crystals from B_{100}. However, at higher cooling rate, Al + Fe^{2+} + Na become significantly more abundant, whilst Fe^{3+} + Mg + Ca decrease (Fig. 2S). At 1 to 7 °C/h, cpx is mainly composed by the Di + En solid solution (Tab. 3b) but, at 60-180 °C/h plg disappears, and Di in cpx importantly decreases counterbalanced by En + Fs + Jd + CaTs increasing (Fig. 6S). The shift from *equilibrium* to *disequilibrium* crystallization is also supported by the change from faceted to dendritic shapes of cpx at 60-180

°C/h (Giuliani et al. 2020b), a feature suggesting a diffusion-controlled regime favoring crystal nucleation rather than growth (Dowty, 1980; Kirkpatrick, 1981; Hammer, 2008).

Figs. 6 and 10S show a quantitative evaluation of *equilibrium versus disequilibrium* crystallization of cpx by employing the value of $^{cpx\text{-}melt}Kd_{Fe\text{-}Mg}$ calculated for the B_{100} bulk composition, according to Putirka et al., (1996). At 1–60 °C/h, cpx approaches to the chemical *equilibrium* condition ($^{cpx\text{-}melt}Kd_{Fe\text{-}Mg}$ = 0.28 ± 0.08), whereas a departure from the chemical *equilibrium* is observed at 180-1800 °C/h (at these conditions plg is absent) (Fig. 6). The lack of plg under fast cooling rate implies that the crystallizing bulk (crystal ± melt) system changes from plg-bearing to plg-absent, making more cations available for the remaining and more stable minerals. However, at 180-1800 °C/h, incompatible and abundant cations like Al (especially in absence of plg) are more favorably incorporated into the dendritic cpx crystals. The strength of the Si-O bonds in the melt (443 kJ/mol) is greater than that of Al-O bonds (330-422 kJ/mol) accounting for the influence of charge-balancing metal cations (e.g. Ca, Na, etc.) on the bonding forces of Al in tetrahedral coordination and the lower charge of trivalent Al compared to tetravalent Si (Kirkpatrick, 1983). This difference in bonding energy implies that the transfer rates of Al cations from the melt to the surface of rapidly growing cpx increases under diffusion-controlled crystal-growth conditions, leading to systematic Al enrichments in the lattice site (Iezzi et al., 2014).

Similarly to cpx, we have also evaluated the *disequilibrium* state of plg using the $^{plg\text{-}melt}Kd_{An\text{-}Ab}$ model proposed by Putirka et al. (2008). Due to the absence of a residual glass in the run products containing plg, and considering that plg is the last crystallizing phase, we applied the *equilibrium* test for plg using both the B_{100} bulk composition and the intra-crystalline glass composition analyzed at 180 °C/h (Tab. 3d, Figs. 6 and 10S). The latter may simulate the composition of a hypothetical residual melt where plg could have crystallized from. Results show that plg is invariably out of the *equilibrium* range as suggested by equilibrium K_d values of 0.15 -

0.05 in Figs. 6 and 10S. Perhaps, this explains why An content in plg remains almost constant under both slow and fast cooling rate conditions (Fig. 3c).

Using cpx-based (error ± 32 °C) and plg-based (error ± 36 °C) thermometers from Putirka et al. (2008), we have verified that the crystallization of plg takes place at temperatures statistically much lower than those of clinopyroxene (Figs. 6 and 11S), when the crystal content is high and the diffusion of cations in the melt is slow due to the higher viscosity. Under such conditions, the system cannot easily return to homogeneous concentrations over the effect of an ever-changing temperature caused by cooling rate and, consequently, plg more effectively records the *disequilibrium* partitioning of cations between the growing crystal surface and the diffusive melt (Fig. 6; Lormand et al., 2021).

Temperature estimates agree with previous textural observations of Vetere et al. (2015) and Giuliani et al. (2020b), suggesting that, considering our experimental conditions, the order of mineral segregation is sp, cpx, and plg. This scenario explains the decreasing trend of Al_2O_3 of plg in the B_{100} contrarily to that of glass-bearing trachybasaltic run-products (Fig. 1c) and on what observed in other more evolved liquids (Mazzi et al., 2008; 2011; 2014). The progressive enrichment of Al at high rates in early grown sp and cpx depleted it from the residual melt from whom plg crystallized (Figs. 1a, 1b, 1c). Also, at high cooling rates, the low degree of crystallization indicates that sp forms homogeneously from the melt and favors the heterogeneous nucleation of cpx (Giuliani et al., 2020b). It is finally worthy of note that despite plg crystals are the latest crystallizing phase, they show the maximum crystal sizes (949-109 µm) and the most abundant crystal contents (65.6 - 46.1 area%). This points out that largest crystals are not necessarily the first to grow from natural MORB melts, or that they are not unequivocally interpretable like phenocrysts or microphenocrysts in volcanic rocks (Kuritani, 1999; Vetere et al., 2015; Giuliani et al., 2020b).

Recent studies on the crystallization of cpx and plg from trachybasalt of the 2001 Mt Etna eruption, were performed in real time from 1250 °C to either 1170 and 1150 °C applying a cooling

rate of 1440 °C/h and then a dwell of 4 h (Polacci et al., 2018 and Arzilli et al., 2019). Results shows that blocky and prismatic cpx and sp crystals grew early. In experiments at 1170 and 1150 the amount of cpx and sp were 1 - 8 and 8 - 8 vol.%, respectively. After a dwell of 4 h, an identical cooling rate was re-applied showing rapid crystallization events of both plg and cpx. During this second cooling event, authors report skeletal growths of plg, between 1112 and 1073 °C for the experiment cooled from 1150 °C and between 1131 and 1053°C for the experiment cooled from 1170°C (Polacci et al., 2018 and Arzilli et al., 2019). Plg crystals grew to *equilibrium* abundance (~ 10 vol.%) in ~ 90 seconds and after the first pulse of plg growth, cpx starts to growth in a dendritic fashion on plg until they reach a final abundance of ~ 65 vol.% in only 180 seconds. At this time sample was fully crystallized suggesting very fast nucleation and growth processes.

Recently, Kolzenburg et al., (2018a; 2018b; 2020), Tripoli et al., (2019), Vetere et al., (2019; 2020a; 2020b) performed studies on the role of shear rate effect in crystals nucleation and growth process. Both agree with the fact that stirring and/or mechanic perturbation enhance nucleation and crystal growth. This is due to a continuous available amount of feed growth ingredients, i.e. elements necessary to build a crystalline structure, favored by the presence of a shear rate (Petrelli et al. 2016; Vetere et al., 2020b). Also, experiments on dynamic crystallization performed on a shoshonitic composition, show a rapid crystals growth rate on the order of ~ 1-2 $\times 10^{-6}$ cm/s (Vetere et al., 2020a). Finally, it is also emerging that relatively high fO_2 determines a relative high delay in nucleation and low temperature onset of nucleation, due to the more viscous and less diffusive properties of ferric-rich silicate melts (Kolzenburg et al., 2018a; 2020).

4.6 Models for MORB solidification

The crystal-chemical outcomes obtained in this study, coupled with the textural and numerical results of Giuliani et al. (2020a, 2020b), allow to define hypothetical models for MORB lavas solidifying under the effect of controlled cooling rate (Fig. 7). The thickness of MORB lava flows

can vary from cm to m, experiencing cooling rates from ≤ 10^0 °C/h to > 10^3 °C/h (Flynn and Mouginis-Mark 1992; Harris et al. 2005; Keszthelyi 1995; Cashman et al. 1999). Using two hypothetical thicknesses of 0.5 and 1.5 m (Fig. 7), we retrieved the cooling regimes of solidification from the numerical simulations conducted by Giuliani et al. (2020a). These conductive cooling models are based on an explicit finite-difference scheme (e.g. Wohletz et al., 1999, and references therein). The following conditions were assumed in the calculations: (i) an initial temperature of 1300 °C for the melt, (ii) a specific heat and thermal conductivity of 1300 J/kgK and 0.9 W/mK; and (iii) a density of 2750 kg/m^3 for the MORB melt (Vetere et al., 2015, Giuliani et al., 2020a, 2020b). The latent heat of crystallization and heat convective transfer was assumed negligible. The cooling regimes have been related to the textural (Tab. 4 and Giuliani et al., 2020b) and crystal-chemical outcomes. To the phase abundance (area%), L_{max} (μm), and G_{CSD} measurements (Tab. 4), we add the number crystal per area (#/A, μm^{-2}), and the cpx-CSDs (Fig. 7). Moreover, the chemical results of this work, basing on the linear regressions followed by some oxides, cations, or components (Figs. 1, 1S-7S) have been reported. As example, Fig. 7 show as the variations of CaO in cpx, Al_2O_3 in plg, and Fe_2O_3 for sp, derived from WDS/EDS analysis, can be used to retrieve the solidification conditions. Likewise, also cations and components can be used (as examples consider Sp *s.s.* for sp and Di/En+Ts for cpx; Figs. 3 and 5S). Textural, chemical, and numerical results suggest that *disequilibrium* crystallization conditions prevail at the bottom and the top of the lava flows, while in their inner parts, crystals grow close to *equilibrium* conditions.

From a rheological point of view, data provided here could be useful to better understand the rheological evolution of a basaltic magma undergoing cooling. Starting with the fact that T_m (melting temperature) is 1218 °C as computed by using alphamelts 1.9 (Asimow and Ghiorso 1998; Ghiorso et al., 2002; Smith & Asimow, 2005) or 1206 °C as measured in Giuliani et al. (2020c), the viscosity is log η = 1.01 (Pa s), according to Giordano et al., (2008). Below T_m a delay in nucleation time is expected as shown above (Polacci et al. 2018; Arzilli et al., 2019). The delay for all the

considered minerals can vary between less than 1 h at ΔT ~ 100 °C to 100 h and more near *liquidus* (ΔT=10/20 °C) (Rusieka et al., 2020). *In situ* differential scanning calorimetry (DSC) technique has been applied to investigate the solidification paths of the identical B_{100} liquid and results straightforward indicate that as the cooling rate increases, the onset temperature of crystal nucleation decreases (Tx_i in Giuliani et al., 2020c). More in details, Tx_i shifts from 1141 to 1086 °C as cooling rate increases from 7 to 1800 °C/h. In this scenario also the melt viscosity changes from 10 to 110 Pa s. After this first steps, nucleation and growth of crystal is rapid (Giuliani et al., 2020b and c) and cause a further quick jump in viscosity (Vona et al., 2011; Kolzenburg et al., 2018a; 2018b; 2020; Vetere et al., 2020a; 2020b). The progressive increasing of crystal content coupled with the progressive enrichment of SiO_2 in the residual melt will be then driven by the crystallization behavior at variable cooling rates.

Cooling conditions in lavas, pillows or dikes are a function of heat dissipation; heat removing depends on thickness, silicate liquid composition and thermal environment of surrounding medium (Giuliani et al., 2002a). In turn, cooling rates decreases moving from outermost to innermost portions, determining flowing in middle portions mainly in response to crystallization behavior and residual melt composition (Figs.1). The early solidified or poorly mobile external portions will be passively transported by innermost parts.

Finally, it has become evident that the formation of Fe-oxide (Fe-rich spinel) nanolites, i.e. crystals lesser than one micron, can affect the rheological properties of melts and drive nucleation and growth processes of large crystals (Vetere et al., 2015; Di Genova et al. 2017, 2018 and 2020 and reference therein). The analytical results presented here derive from experiments that span a wide range of cooling rates. Under fast rates it is evident the formation of sp nanolites (Giuliani et al., 2020b), although their actual composition is not measured here due to their tiny sizes (Fig. 1a). Micro-chemical characterizations with TEM are under development to bracket this aspect. At low

cooling rates it remains an open question if crystallization also initiates by an early appearance of such sub-micrometric sp phases.

5. Conclusions

In this study, the mineral compositional changes of sp, cpx, and plg formed from an actual, homogeneous and seed-free MORB melt have been measured (Figs. 1,2) and then integrated with the textural parameters (Figs. 3,4). Both these measurements involve experimental charges solidified at cooling rates variable from 1 to 9000 °C/h, applied from *superliquidus* to *solidus* conditions. Our experiments albeit run at air testify general common behaviors with previous investigations (Figs. 1). The bulk chemical system and fO_2 plays a significant role in crystal-chemical differences observed in early formed sp (Fig. 1a). Conversely, cpx is less affected by whole chemical systems and fO_2 (Fig. 1b). The composition of lately formed plg is strongly dependent to the presence or absence of a residual liquid. Therefore, cpx is the most useful phase to retrieve kinetics of dynamic solidification conditions occurring at low and high cooling rates, at least at moderate to high fO_2 conditions.

The following conclusions can be drawn:

1) the chemistry of sp, cpx and, to a minor extent, of plg is quantitatively related to the cooling rate condition, with emphasis for the preferential incorporation of incompatible cations in the lattice site with increasing cooling rate;

2) several oxides, and consequently cations, and components, in minerals are found to be linearly correlated with cooling rate, showing very good statistics regression that provide robust geospeedometers for MORB rocks;

3) the crystal growth rates (G_{max} and G_{CSD}) measured by textural analysis can be retrieved also by the mineral compositional changes, strengthening the observation that the solidifying system shifts from interface-controlled to diffusion-controlled growth regimes with increasing cooling rate;

4) at cooling rate ≤ 60 °C, the crystallization of cpx takes place under near-*equilibrium* conditions, albeit plg systematically crystallizes in *disequilibrium* regimes. This phenomenon pairs with the late saturation of plg and the slow diffusion of cations in the melt phase, which takes place at a temperature much lower than that of cpx;

5) overall, as cooling rate increases by 3/4 orders of magnitude, there is a close relationship between the textural maturation of cpx and its chemistry. Because of its abundance, large crystal size, and great stability, we conclude that cpx is the most suitable mineral phase to monitor the crystallization kinetics of naturally cooled MORB melts;

6) the application of geospedometers is a function of the silicate liquid, either initial or residual, from where a mineral grows; in turn, the order of mineral segregation and the presence of glass have to be evaluated.

The quantitative relationships found in this work, coupled with previous textural and numerical results furnish novel geo-speedometers for MORB melt at atmospheric fO_2 and allows us to bracket quantitative solidification models for dry and aphyric MORB lavas with variable thicknesses.

Figure 1S. Cation abundances (a.p.f.u.) in spinel (sp) as a function of $\Delta T/\Delta t$ (°C/h). Average data are listed in Tab. 3Sa. The 95% confidence interval refers to the average chemical values measured for crystals solidified at different cooling rates.

Figure 2S. Cation abundances (a.p.f.u.) in clinopyroxene (cpx) as a function of $\Delta T/\Delta t$ (°C/h). Average data are listed in Tab. 3Sb. Only linear regressions with $R^2 \geq 0.60$ are plotted. The 95% confidence interval refers to the average chemical values measured for crystals solidified at different cooling rates.

Figure 3S. Variations of Fe^{2+}/Fe^{tot} and Mg# in clinopyroxene (cpx) as a function of $\Delta T/\Delta t$ (°C/h). Average data are listed in Tab. 1Sb.

Figure 4S. Cation abundances (a.p.f.u.) in plagioclase (plg) as a function of $\Delta T/\Delta t$ (°C/h). Average data are listed in Tab. S1c. Only linear regressions with $R^2 \geq 0.60$ are plotted. Mg is not plotted because its content is on average less than 0.01 a.p.f.u.. The 95% confidence interval refers to the average chemical values measured for crystals solidified at different cooling rates.

Figure 5S. Component changes (mol %) in spinel (sp) as a function of $\Delta T/\Delta t$ (°C/h). Sp *s.s.* = Spinel *sensu stricto* ($^{T}Mg^{M}Al_2O_4$), Mag = Magnetite ($^{T}Fe^{3+M}Fe^{2+}\ ^{M}Fe^{3+}O_4$), Usp = Ulvospinel ($^{T}Fe^{2+M}Fe^{2+}\ ^{M}Ti^{4+}O_4$). Average data are listed in Tab. S1a. Only linear regressions with $R^2 \geq 0.60$ are plotted. The 95% confidence interval refers to the average chemical values measured for crystals solidified at different cooling rates.

Figure 6S. Component changes (mol.%) in clinopyroxene (cpx) as a function of $\Delta T/\Delta t$ (°C/h). Di = diopside ($^{M2}Ca^{M1}Mg^{T}Si_2O_6$), En = enstatite ($^{M2}Mg^{M1}Mg^{T}Si_2O_6$), Fs = ferrosilite ($^{M2}Fe^{2+M1}Fe^{2+T}Si_2O_6$), Hd = hedenbergite ($^{M2}Ca^{M1}Fe^{2+T}Si_2O_6$), Jd = jadeite ($^{M2}Na^{M1}Al^{T}Si_2O_6$), CaTs = Ca-Tschermak ($^{M2}Ca^{M1}Al^{T}(SiAl)O_6$), CaTs = CaFe-Tschermak ($^{M2}Ca^{M1}Fe^{3+T}(SiFe^{3+})O_6$) and CaTiTs = CaTi-Tschermak ($^{M2}Ca^{M1}Ti^{T}(SiTi)O_6$). Average data are listed in Tab. 3Sb. Only linear regressions with $R^2 \geq 0.6$ are plotted. The 95% confidence interval refers to the average chemical values measured for crystals solidified at different cooling rates.

Figure 7S. Component changes (mol.%) in plagioclase (plg) as a function of $\Delta T/\Delta t$ (°C/h). Ab = Albite ($^{M}Na^{T}(AlSi_3)O_8$), An = Anorthite ($^{M}Ca^{T}(Al_2Si_2)O_8$). Average data are listed in Tab.

S1c. The 95% confidence interval refers to the average chemical values measured for crystals solidified at different cooling rates.

Figure 8S. Classification diagrams for sp, cpx and plg (average data in Tabs. 3Sa, b, c, respectively; acronyms correspond to: Sp *s.s.* = spinel *sensu stricto* ($^{T}Mg^{M}Al_2O_4$), Mag = magnetite ($^{T}Fe^{3+M}(Fe^{2+}Fe^{3+})O_4$), Usp = ulvospinel ($^{T}Fe^{2+M}(Fe^{2+}Ti^{4+})O_4$), Di = diopside ($^{M2}Ca^{M1}Mg^{T}Si_2O_6$), Hd = hedenbergite ($^{M2}Ca^{M1}Fe^{2+T}Si_2O_6$), En = enstatite ($^{M2}Mg^{M1}Mg^{T}Si_2O_6$), Fs = ferrosilite ($^{M2}Fe^{2+M1}Fe^{2+T}Si_2O_6$), Ab = albite ($^{M}Na^{T}(AlSi_3)O_8$), An = anorthite ($^{M}Ca^{T}(Al_2Si_2)O_8$) and Or = orthoclase ($^{M}K^{T}(AlSi_3)O_8$).

Figure 9S. Relationships between phase amount measured by image analysis as area% and measured by mass balance from average oxide wt.% compositions.

Figure 10S. Relative distributions (%) of the partitioning coefficients between cpx and plg-core and melt (i.e. $^{cpx\text{-}melt}Kd_{Fe\text{-}Mg}$ and $^{plg\text{-}melt}Kd_{Ab\text{-}An}$, respectively). (*Dis*)*equilibrium* conditions have been tested following the model proposed by Putirka et al., 1996 for cpx and following Putirka et al., 2008, for plg. We considered 20 bins for $^{cpx\text{-}melt}Kd_{Fe\text{-}Mg}$, covering a range from 0 to 1, and 20 bins for $^{plg\text{-}melt}Kd_{Ab\text{-}An}$, involving a range from 0 to 2 (in both the cases, the bin size is 0.1). Yellow areas indicate the *equilibrium* ranges.

Figure 11S. Relative distributions (%) of the crystallization temperatures, estimated for cpx and plg (Putirka et al., 2008). We considered 25 bins for *T* of cpx, covering a range from 1350 to 1100 °C, and 10 bins for *T* of plg, covering a range from 950 to 850 °C (in both the cases, the bin size is 10 °C).

Declaration of Competing Interest

The authors declare that they have not competing financial interests or personal relationships that could have appeared to influence the work reported in this paper.

Acknowledgments

The authors would like to thank the editor and the reviewers for their handling. This study was funded by the "Fondi Ateneo of the University G. D'Annunzio", PRIN (2009PZ47NA_003) project "Experimental determination of the glass-forming ability (GFA), nucleation and crystallization of natural silicate melts" and PRIN (2017J277S9_003) project "Time scales of solidification in magmas: Application to Volcanic Eruptions, Silicate Melts, Glasses, Glass-Ceramics" awarded to G. Iezzi. Most of this study was conducted during the Ph.D. of L. Giuliani. Alexander von Humbold foundation senior research grant to F. Vetere is also acknowledged.

References

Arzilli, F., La Spina, G., Burton, M.R., Polacci, M., Le Gall, N., Hartley, M.E., Di Genova, D., Cai, B., Vo, N.T., Bamber, E.C. and Nonni, S., 2019. Magma fragmentation in highly explosive basaltic eruptions induced by rapid crystallization. Nature Geoscience, 12(12), pp.1023-1028.

Asimow, P. D., and Ghiorso M. S., 1998. Algorithmic modifications extending MELTS to calculate subsolidus phase relations. American Mineralogist, 83, 1127-1132.

Bagiński, B., Dzierżanowski, P., Macdonald, R., and Upton B. G. J., 2009. Complex relationships among coexisting pyroxenes: the Palaeogene Eskdalemuir dyke, Scotland. Mineralogical Magazine, 73, 929 – 242.

Baker, M.B. and Grove, T.L., 1985. Kinetic controls on pyroxene nucleation and metastable liquid lines of descendent in a basaltic andesite. American Mineralogist, 70, 279 – 287.

Ballhaus, C., 1993. Redox States of Lithospheric and Asthenospheric Upper-Mantle, Contributions to Mineralogy and Petrology, 114(3), 331-348.

Behrens, H., Misiti., V., Freda, C., Vetere, F., Botcharnikov, R.E., Scarlato, P., 2009. Solubility of H_2O and CO_2 in ultrapotassic melts at 1200 and 1250 °C and pressure from 50 to 500 MPa. American Mineralogist, 94:105–120.

Bezos, A., Guivel, C., La C., Fougeroux, T., Hulmer, F., 2021. Unraveling the confusion over the iron oxidation state in MORB glasses. Geochimica et Cosmochimica Acta, 293, 28-39

Burgisser, A. and Scaillet, B., 2007. Redox evolution of a degassing magma rising to the surface. Nature, 445, 194-197.

Canil, D., 1997. Vanadium partitioning and the oxidation state of Archaean komatiite magmas. Nature, 389(6653), 842-845.

Carmichael, I. S. E., 1991. The Redox States of Basic and Silicic Magmas - a Reflection of Their Source Regions, Contributions to Mineralogy and Petrology, 106(2), 129-141.

Cashman, K.V., Thornber, C., Kauahikaua, J.P., 1999. Cooling and crystallization of lava in open channels, and the transition of Pāhoehoe Lava to 'A'ā. Bulletin of Volcanology, 61(5):306-323

Chadima, M., Cajz, V. and Týcová P., 2009. On the interpretation of normal and inverse magnetic fabric in dikes: Examples from the Eger Graben, NW Bohemian Massif. Tectonophysics, 466, 47–63. doi: 10.1016/j.tecto.2008.09.005.

Chistyakova, S. Y. and Latypov, R. M., 2009. Two independent processes responsible for compositional zonation in mafic dykes of the Åland-Åboland Dyke Swarm, Kestiö Island, SW Finland. Lithos, 112, 382 – 396. doi:10.1016/j.lithos.2009.03.037.

Christie, D. M., Carmichael I. S. E., and Langmuir C. H., 1986. Oxidation-States of Midocean Ridge Basalt Glasses. Earth and Planetary Science Letters, 79(3-4), 397-411.

Coish, R.A. and Taylor, L.A., 1979. The effects of cooling rate on texture and pyroxene chemistry in DSDP LEG 34 basalt: a microprobe study. Earth and Planetary Science Letters, 42, 389 - 398.

Conte, A.M., Perinelli, C. and Trigila, R., 2006. Cooling kinetics experiments on different Stromboli lavas: Effects on crystal morphologies and phases composition. Journal of Volcanology and Geothermal Research, 155 (3-4), pp.179- 200.

Cottrell, E., Birner, S., Brounce, M. Davis, F. A. Waters L. E. and Kelley K. A., 2021. Oxygen Fugacity Across Tectonic Settings. AGU Geophysical Monograph Series Redox variables and mechanisms in magmatism and volcanism. Editors: Neuville, D. R. and Moretti, R. Wiley. doi:10.1002/9781119473206.ch3.

Couch, S., 2003. Experimental investigation of crystallization kinetics in a haplogranite system. American Mineralogist, 88, 1471 – 1485.

Crisp, J.A., 1984. Rates of magma emplacement and volcanic output. Journal of Volcanology and Geothermal Research, 20, 177–211. doi:10.1016/0377-0273(84)90039-8.

Deer, W.A., Howie, R. A. and Zussmann, J., 1997. Rock-forming minerals. Single-Chain Silicates. Second Edition. The Geological Society.

Del Gaudio, P., Mollo, S., Ventura, G., Iezzi, G., Taddeucci, J. and Cavallo, A., 2010. Cooling rate-induced differentiation in anhydrous and hydrous basalts at 500 MPa: Implications for the storage and transport of magmas in dikes. Chemical Geology, 270, 164 – 178.

Della Ventura, G., Iezzi, G., Redhammer, G.J., Hawthorne, F.C., Scaillet, B., Novembre, D., 2005. Synthesis and crystal-chemistry of amphiboles along the magnesioriebeckite – magnesio-arfvedsonite series as a function of fO2. American Mineralogist, 90: 1375-1383.

Di Genova, D., Brooker, R. A., Mader, H. M., Drewitt, J. W. E., Longo, A., Deubener, J., Neuville, D. R., Fanara, S., Shebanova, O., Anzellini, S., Arzilli, F., Bamber, E. C., Hennet, L., La Spina, G., Miyajima, N., 2020. In situ observation of nanolite growth in volcanic melt: A driving force for explosive eruptions. Science Advances, 6(39): eabb0413.

Di Genova D, Hess K-U, Oryaëlle Chevrel M, Dingwell D.B., 2016. Models for the estimation of Fe3+/Fetot ratio in terrestrial and extraterrestrial alkali-and iron-rich silicate glasses using Raman spectroscopy. American Mineralogist 101(4):943-952

Di Genova, D., Kolzenburg, S., Wiesmaier, S., Dallanave, E., Neuville, D. R., Hess, K. U., Dingwell, D. B., 2017. A compositional tipping point governing the mobilization and eruption style of rhyolitic magma. Nature 552:235.

Di Genova D, Caracciolo A, Kolzenburg S., 2018. Measuring the degree of "nanotilization" of volcanic glasses: Understanding syn-eruptive processes recorded in melt inclusions. Lithos 318-319:209-218.

Dingwell, D.B., 2006. Transport properties of magmas: diffusion and rheology. Elements, 2, 281 – 286.

Dowty, E., 1980. Crystal growth and nucleation theory and the numerical simulation of igneous crystallization. Pp. 419-485 in: The Physics of Magmatic Processes (Hargraves R.B., editor) Princeton University Press, Princeton, New Jersey, USA.

Dunbar, N. W., Jacobs, G. K. and Naney, M. T., 1995. Crystallization processes in an artificial magma: variations in crystal shape, growth rate and composition with melt cooling history. Contribution to Mineralogy and Petrology 120, 412 – 425.

Eugster, H., 1957. Heterogeneous reactions involving oxidation and reduction at high pressures and temperatures. The Journal of Chemical Physics, 26(6), 1760-1761.

Eugster, H. P., 1959. Oxidation and reduction in metamorphism. John Wiley & Sons, New York 397-426 pp.

Flanagan, F.J., 1984. Three USGS mafic rock reference samples, W-2, DNC-1, and BIR-1: U.S. Geological Survey Bulletin 1623, 54 p.

Flynn, L. P., Mouginis-Mark, P. J., 1992. Cooling rate of an active Hawaiian lava flow from nighttime spectroradiometer measurements. Geophysical Research Letters 19(17):1783- 1786.

Frost, B. R. and Lindsley, D. H., 1992. Equilibria among Fe-Ti oxides, pyroxenes, olivine, and quartz 2. American Mineralogist, 77(9-10), 1004-1020.

Gale, A., Dalton, C.A., Langmuir, C.H., Su, Y., Schilling, J.G., 2013. The mean composition of ocean ridge basalts. Geochemistry Geophysics Geosystem, 14. doi:10. 1029/2012GC004334.

Gamble, R. P. and Taylor, L. A., 1980. Crystal/liquid partitioning in augite: effects of cooling rate. Earth and Planetary Science Letters. 47, 21 – 33.

Ghiorso, M. S., Hirschmann, M. M., Reiners, P. W. and Kress V. C., 2002. The pMELTS: A revision of MELTS for improved calculation of phase relations and major element partitioning related to partial melting of the mantle to 3 GPa, Geochemistry Geophysics Geosystem, 3, 1030.

Giordano, D., Russell, J. K. and Dingwell, D. B., 2008. Viscosity of magmatic liquids: a model. Earth and Planetary Science Letters, 271, 123–134. doi.org/10.1016/j.epsl.2008.03.038

Giuliani, L., Iezzi, G. and Mollo, S., 2020a. Dynamics of volcanic systems: physical and chemical models applied to equilibrium versus disequilibrium solidification of magmas. In: "Dynamic Magma Evolution" Geophysical Monograph. First Edition. American Geophysical Union. Published by John Wiley & Sons. ISBN:987-1-119-52113-6.

Giuliani, L., Iezzi, G., Hippeli, T., Davis, M., Elbrecht, A., Vetere, F., Nazzari, M. and Mollo, S., 2020c. The onset and solidification path of a basaltic melt by in situ differential scanning

calorimetry (DSC) and ex situ investigations. Frontiers in Earth Sciences, 8:337. doi: 10.3389/feart.2020.00337.

Giuliani, L., Iezzi, G., Vetere, F., Behrens, H., Mollo, S., Cauti, F., Ventura, G. and Scarlato P., 2020b. Evolution of textures, crystal size distributions and growth rates of plagioclase, clinopyroxene and spinel solidified at variable cooling rates from a mid-ocean ridge basaltic liquid. Earth Science Review, 204, 103165.

Grove, T. L. and Bence A. E., 1979. Crystallization kinetics in a multiply saturated basalt magma: an experimental study of Luna 24 ferrobasalt. Proceeding Lunar Science Conference 10th, 439 – 478.

Grove, T. L. and Raudsepp, M., 1978. Effects of kinetics on the crystallization of quartz normative basalt 15597: an experimental study. Proceeding Lunar Science Conference 9th. 585 – 599.

Haggerty, S., 1976. Opaque mineral oxides in terrestrial igneous rocks, Oxide minerals. Short course notes, 3.

Hammer, J. E., 2006. Influence of fO_2 and cooling rate on the kinetics and energetics of Fe – rich basalt crystallization. Earth and Planetary Science Letters, 248, 618 – 637.

Hammer, J. E., 2008. Experimental studies of the kinetics and energetics of magma crystallization. In: Putirka K. D. and Tepley F. J. (Eds.). Review in Mineralogy and Geochemistry, 69, 9 – 59.

Hammer, J. E., 2009. Capturing crystal growth. Geology, 37, 1055 – 1056. doi: 10.1130/focus112009.1.

Harris, A., Bailey, J., Calvari, S. and Dehn, J., 2005. Heat loss measured at a lava channel and its implications for down-channel cooling and rheology. Special paper- Geological Society of America 396:125

Heltz, R. and Thornber, C., 1987. Geothermometry of Kīlauea Iki lavas, Hawaii. Bulletin of Volcanology, 49:651-668

Keszthelyi, L., 1995. Measurements of the cooling at the base of pahoehoe flows. Geophysical Research Letters, 22(16):2195-2198.

Iezzi, G., Boffa-Ballaran, T., McCammon, C., Langenhorst, F., 2005. The $CaGeO_3$-$Ca_3Fe_2Ge_3O_{12}$ garnet solid solution. Physics and Chemistry of Minerals, 32: 197-207.

Iezzi, G., Mollo, S., Ventura, G., Cavallo, A. and Romano, C., 2008. Experimental solidification of anhydrous latiti and trachytic melts at different cooling rates: the role of nucleation kinetics. Chemical Geolology, 253, 91 – 101. doi: 10.1016/j.chemgeo.2008.04.008.

Iezzi, G., Mollo, S. and Ventura, G., 2009. Solidification behavior of natural silicate melts and volcanological implications. In: Lewis N. and Moretti A. (Eds.), Volcanoes: formation, eruptions and modeling. Nova publishers, New York, 127 – 151.

Iezzi, G., Mollo, S., Torresi, G., Ventura, G., Cavallo, A. and Scarlato P., 2011. Experimental solidification of an andesitic melt by cooling. Chemical Geology 283, 261 – 273. doi: 10.1016/j.chemgeo.2011.01.024.

Iezzi, G., Mollo, S., Shahin, E., Cavallo A. and Scarlato, P., 2014. The cooling kinetics of plagioclase feldspar as revealed by electron-microprobe mapping. American Mineraloist, 99, 898 – 907. doi: http://dx.doi.org/10.2138/am.2014.4626.

Iwamori, H. and Nakamura, H., 2015. Isotopic heterogeneity of oceanic, arc and continental basalts and its implications for mantle dynamics. Gondwana Research. 27, 1131 – 1152. http://dx.doi.org/10.1016/j.gr.2014.09.003.

Kennedy, G. C., 1955. Some Aspects of the Role of Water in Rock Melts. Geological Society of America Special Paper, 62, 489-504.

Kirkpatrick, R. J., 1981. Kinetics of crystallization of igneous rocks. In: Lasaga A. C. and Kirkpatrick R. J., (Eds.). Review in Mineralogy and Geochemistry, 8, 321 – 397.

Kirkpatrick, R. J., 1983. Theory of nucleation in silicate melts. American Minerlogist, 68, 66 – 77.

Kissell, C., Laj, C., Sigurdsson, H. and Guillou, H., 2010. Emplacement of magma in Eastern Iceland dikes. Insights from magneti fabric and rock magnetic analysis. Journal of Volcanology and Geothermal Research, 191, 79 – 92.

Kolzenburg, S., Giodano, D., Hess, K. U. and Dingwell, D. B., 2018a. Shear Rate-Dependent Disequilibrium Rheology and Dynamics of Basalt Solidification. Geophysical Research Letters 45(13):6466-6475.

Kolzenburg, S., Di Genova, D., Giordano, D., Hess, K. U. and Dingwell, D. B., 2018b. The effect of oxygen fugacity on the rheological evolution of crystallizing basaltic melts. Earth and Planetary Science Letters, 487:21-32.

Kolzenburg, S., Hess, K. U., Berlo, K. and Dingwell, D. B., 2020. Disequilibrium Rheology and Crystallization Kinetics of Basalts and Implications for the Phlegrean Volcanic District. Frontiers in Earth Science, 8(187)

Kouchi, A., Tsuchiyama, A., Sunagawa, I., 1986. Effect of stirring on crystallization kinetics of basalt: texture and element partitioning. Contributions to Mineralogy and Petrology 93(4):429-438

Kress, V. C. and Carmichael, I. S. E., 1991. The compressibility of silicate liquids containing Fe_2O_3 and the effect of composition, temperature, oxygen fugacity and pressure on their redox states. Contribution to Mineralogy and Petrology, 108, 82–92

Kuritani, T., 1999. Phenocryst crystallization during ascent of alkali basalt magma at Rishiri Volcano, northern Japan. Journal of Volcanology and Geothermal Research, 88, 77–97.

Lormand, C., Zellmer, G.F., Sakamoto, N. et al. 2021. Shallow magmatic processes revealed by cryptic microantecrysts: a case study from the Taupo Volcanic Zone. Contrib Mineral Petrol 176, 97. doi:10.1007/s00410-021-01857-7

Lasaga, A. C., 1998. Kinetic theory in the Earth Sciences. Princeton university press, Princenton, New York.

Lesher, C. E., Cashman, K. V. and Mayfield, J. D., 1999. Kinetic controls on crystallization of Tertiary North Atlantic basalt and implications for the emplacement and cooling history of lava at Site 989, Southeast Greenland rifted margin. In: Larsen H.C., Duncan R.A., Allan J.F., Brooks K. (Eds.), Proceeding of ODP Scientific results, 163, 135 – 148.

Lofgren, G. E., Huss, G. R. and Wasserburg, G. J., 2006. An experimental study of trace-element partitioning between Ti-Al-clinopyroxene and melt: Equilibrium and kinetic effects including sector zoning. American Mineralogist, 91, 1596 – 1606 doi: 10.2138/am.2006.2108

Maclennan, J., 2019. Mafic tiers and transient mushes: evidence from Iceland. *Phil. Trans. R. Soc. A* **377**: 20180021. http://dx.doi.org/10.1098/rsta.2018.0021

Masotta, M., Pontesilli, A., Mollo, S., Armienti, P., Ubide, T., Nazzari, M. and Scarlato, P., 2020. The role of undercooling during clinopyroxene growth in trachybasaltic magmas: Insights on magma decompression and cooling at Mt. Etna volcano. Geochimica et Cosmochimica Acta, 268, 258-276.

Matsui, Y., Onuma, N., Nagasawa, H., Higuchi, H., Banno, S., 1977. Crystal structure control in trace element partition between crystal and magma. Tectonics, 100, 315–324

McGuire, A.V., Dyar, M.D. and Ward, K., 1989. Neglected Fe^{3+}/Fe^{2+} ratios—a study of Fe3+ content of megacrysts from alkali basalts. Geology, 17, 687–690.

Mevel, C. and Velde D., 1976. Clinopyroxenes in Mesozoic pillow lavas from the French Alps: influence of cooling rate on compositional trends. Earth and Planetary Science Letters. 32, 158 – 164.

Mollo, S. and Hammer, J. E., 2017. Dynamic crystallization in magmas. In: EMU Notes in Mineralogy, 16, 373 – 418. doi:10.1180/EMU-notes.16.12.

Mollo, S., Del Gaudio, P., Ventura, G., Iezzi, G. and Scarlato P., 2010. Dependence of clinopyroxene composition on cooling rate in basaltic magmas: implications for thermobarometry. Lithos, 118, 302 – 312.

Mollo, S., Lanzafame, G., Masotta, M., Iezzi, G., Ferlito, C. and Scarlato P., 2011a. Cooling history of a dike as revealed by mineral chemistry: a case study from Mt. Etna volcano. Chemical Geology, 288, 39 – 52.

Mollo, S., Putirka, K., Iezzi, G., Del Gaudio, P. and Scarlato P., 2011b. Plagioclase-melt (dis)equilibrium due to cooling dynamics: implications for thermometry, barometry and hygrometry. Lithos, 125, 221 – 235.

Mollo, S., Misiti, V., Scarlato, P. and Soligo, M., 2012. The role of cooling rate in the origin of high temperature phases at the chilled margin of magmatic intrusions. Chemical Geology, 322, 28 – 46.

Mollo, S., Putirka, K., Misiti, V., Soligo, M. and Scarlato P., 2013a. A new test for equilibrium based on clinopyroxene – melt pairs: clues on the solidification temperatures of Etnean alkaline melts at post-eruptive conditions. Chemical Geology, 352, 92 – 100.

Mollo, S., Putirka, K., Iezzi, G. and Scarlato, P., 2013b. The control of cooling rate on titanomagnetite composition: implications for a geospeedometry model applicable to alkaline rocks from Mt. Etna volcano. Contribution to Mineralogy and Petrology, 165, 457 – 475. doi: 10.1007/s00410-012-0817-6.

Mollo, S., Blundy, J. D., Iezzi, G., Scarlato, P. and Langone, A., 2013c. The partitioning of trace elements between clinopyroxene and trachybasaltic melt during rapid cooling and crystal growth. Contribution to Mineralogy and Petrology, 166, 1633 – 1654. doi: 10.1007/s00410-013-0946-6.

Morimoto, N., 1988. Nomenclature of Pyroxenes. Mineralogy and Petrology, 39, 55 – 76.

O'Donovan, J. B. and O'Reilly, W., 1977. Range of non-stoichiometry and characteristic properties of the products of laboratory maghemitization. Earth and Planetary Science Letters. 34, 291–299. doi:10.1016/0012-821x (77)90013-9.

Osborn, E. F., 1959. Role of Oxygen Pressure in the Crystallization and Differentiation of Basaltic Magma. American Journal of Science, 257(9), 609-647.

Óskarsson, B.V. and Riishuus M.S., 2013. The mode of emplacement of Neogene flood basalts in Eastern Iceland: Facies architecture and structure of the Hólmar and Grjótá olivine basalt groups. Journal of Volcanology and Geothermal Research 267, 92–112

Óskarsson, B.V. and Riishuus M.S., 2014. The mode of emplacement of Neogene flood basalts in eastern Iceland: Facies architecture and structure of simple aphyric basalt groups. Journal of Volcanology and Geothermal Research 289 (2014) 170–192

Óskarsson, B.V., Andersen C. B., Riishuus M. S., Sørensen E.V., Tegner C., 2017. The mode of emplacement of Neogene flood basalts in Eastern Iceland: The plagioclase ultraphyric basalts in the Grænavatn group. Journal of Volcanology and Geothermal Research 332 (2017) 26–50

Petrelli, M., El Omari, K., Le Guer, Y. and Perugini, D., 2016. Effects of chaotic advection on the timescales of cooling and crystallization of magma bodies at mid crustal levels, Geochemistry Geophysics Geosystem, 17, 425–441. doi:10.1002/2015GC006109

Pichavant, M., Costa F., Burgisser, A., Scaillet, B., Martel, C. and Poussineau, S., 2007. Equilibration scales in silicic to intermediate magmas – implications for experimental studies. Journal of Petrology, 48, 1955 – 1972.

Pick, T. and Tauxe, L., 1994. Characteristics of magnetite in submarine basaltic glass. Geophysical Journal Interntional, 119, 116 – 128.

Polacci, M., Arzilli, F., La Spina, G., Le Gall, N., Cai, B., Hartley, M.E., Di Genova, D., Vo, N.T., Nonni, S., Atwood, R.C. and Llewellin, E.W., 2018. Crystallisation in basaltic magmas revealed via in situ 4D synchrotron X-ray microtomography. Scientific reports, 8, 1-13.

Pontesilli, A., Masotta, M., Nazzari, M., Mollo, S., Armienti, P., Scarlato, P. and Brenna, M., 2019. Crystallization kinetics of clinopyroxene and titanomagnetite growing from a trachybasaltic melt: New insights from isothermal time-series experiments. Chemical Geology, 510, 113-129. doi:10.1016/j.chemgeo.2019.02.015.

Pupier, E., Duchene, S. and Toplis, M., 2008. Experimental quantification of plagioclase crystal size distribution during cooling of a basaltic liquid. Contribution to Mineralogy and Petrology, 155, 555 – 570. doi: 10.1007/s00410-007-0258-9.

Putirka, K., Johnson, M., Kinzler, R., Longhi, J. and Walker, D., 1996. Thermobarometry of mafic igneous rocks based on clinopyroxene-liquid equilibria, 0-30 kbar. Contribution to Mineralogy and Petrology, 123, 92 – 108.

Putirka, K., Mikaellian, H., Ryerson, F., and Shaw, H., 2003. New clinopyroxene-liquid thermobarometers for mafic, evolved, and volatile-bearing lava compositions, with applications to lavas from Tibet and the Snake River Plain, Idaho. American Mineralogist, 88, 1542–1554.

Putirka, K.D., 2008. Thermometers and barometers for volcanic systems. In: Reviews in Mineralogy and Geochemistry, 69, 61 – 120.

Roskosz, M., Toplis, M. J. and Richet, P. 2006. Kinetic vs. thermodynamic control of nucleation and growth in molten silicates. Journal of Non-Crystalline solids, 352, 180 – 184.

Roskosz, M., Toplis, M. J., Besson, P. and Richet, P., 2005. Nucleation mechanisms: a crystal chemical investigation of phases forming in highly supercooled aluminosilicate liquids. Journal of Non-Crystalline solids. 351, 1266 – 1282.

Rowe, M.C., Kent, A. J. R. and Nielsen, R. L., 2009. Subduction Influence on Oxygen Fugacity and Trace and Volatile Elements in Basalts Across the Cascade Volcanic Arc. Journal of Petrology, 50, 1-51. doi:10.1093/petrology/egn072.

Rusiecka, M. K., Bilodeau, M., Baker, D. R., 2020. Quantification of nucleation delay in magmatic systems: experimental and theoretical approach. Contributions to Mineralogy and Petrology, 175(5), 47.

Schiavi, F., Walte, N. and Keppler, H., 2009. First in situ observation of crystallization processes in a basaltic – andesitic melt with the moissanite cell. Geology, 37, 963 – 966. doi: 10.1130/G30087A.1.

Shiffman, P. and Lofgren, G. E., 1982. Dynamic crystallization studies on the Grande Ronde Pillow Basalt, central Washington. Journal of Geology, 90, 49-78

Smith, B. M. and Prévot, M., 1977. Variation of the magnetic properties in a basaltic dyke with concentric cooling zones. Physics of the Earth and Planetary Interior. 14, 120 – 136.

Smith, D. and Lindsley, D. H., 1971. Stable and metastable augite crystallization trends in a single basalt flow. American Mineralogist, 56, 225–232.

Smith, V. G., Tiller, W. A. and Rutter, J. W., 1955. A mathematical analysis of solute redistribution during solidification. Canadian Journal of Physics 33, 723–745.

Smith, P. M. and Asimow, P. D., 2005. Adiabat_1ph: A new public front-end to the MELTS, pMELTS, and pHMELTS models. Geochemistry Geophysics Geosystistem, 6, Q02004, doi:10.1029/2004GC000816.

Soule, S.A., 2015. Mid-Ocean Ridge Volcanism. In: Sigurdsson, H., Houghton, B., McNutt, S.R., Rymer, H., Stix, J. (Eds.), The Encyclopedia of Volcanoes, second edition. pp. 395–403. doi:10.1016/B978-0-12-385938-9.00021-3.

Tripoli, B., Manga, M., Mayeux, J., Barnard, H., 2019. The Effects of Deformation on the Early Crystallization Kinetics of Basaltic Magmas. Frontiers in Earth Science 7:250. doi: 10.3389/feart.2019.00250

Tsuchiyama, A., 1985. Crystallization kinetics in the system $CaMgSi_2O_6$-$CaAl_2Si_2O_8$: development of zoning and kinetics effects on element partitioning. American Mineralogist, 70, 474 – 486.

Ujike, O., 1982. Microprobe mineralogy of plagioclase, clinopyroxene and amphibole as records of cooling rate in the Shirotori – Hiketa dike swarm, northeastern Shikoku, Japan. Lithos, 15, 281 – 293.

Vetere, F., Iezzi, G., Beherens, H., Cavallo, A., Misiti, V., Dietrich, M., Knipping, J., Ventura, G. and Mollo, S., 2013. Intrinsic solidification behaviour of basaltic to rhyolitic melts: a cooling rate experimental study. Chemical Geology, 354, 233 – 242.

Vetere, F., Behrens, H., Botcharnikov, R., Holtz, F. and Fanara S., 2014. The role of alkalis in the solubility of H_2O and CO_2 in silicate melts. Implication for phonotephritic magmas. Contribution to Mineralogy and Petrology, 167, 1-17.

Vetere, F., Iezzi, G., Beherens, H., Holtz, F., Ventura, G., Misiti, V., Cavallo, A., Mollo, S. and Dietrich, M., 2015. Glass forming ability and crystallization behaviour of sub – alkaline silicate melts. Earth-Science reviews. 150, 25 – 44.

Vetere, F., Murri, M., Alvaro, M., Domeneghetti, M. C., Rossi, S., Pisello, A., Holtz, F. and Perugini D., 2019. Viscosity of Pyroxenite Melt and its Evolution during Cooling: an experimental approach. Journal of Geophysics Research-Planets, 124. doi: 10.1029/2018JE005851

Vetere, F., Mazzeo, A., Perugini, D. and Holtz, F., 2020a. Viscosity behaviour of silicate melts during cooling under variable shear rates. Journal of Non-Crystalline Solids, 533, 119902.

Vetere, F. and Holtz, F., 2020b. Rheological behavior of partly crystallized silicate melts under variable shear rate. Chapter in Dynamic Magma Evolution, Geophysical Monograph Series – WILEY, edited by Vetere, F.

Villeneuve, N., Neuville, D. R., Boivin, P., Bachèlery, P. and Richet, P., 2008. Magma crystallization and viscosity: a study of molten basalts from the Piton de la Fournaise volcano (La Réunion island). Chemical Geology, 256, 241 – 250.

Vona, A., Romano, C., Dingwell, D. B., & Giordano, D., 2011. The rheology of crystal-bearing basaltic magmas from Stromboli and Etna. Geochimica et Cosmochimica Acta, 75(11), 3214–3236. doi:10.1016/j.gca.2011.03.031

Wallace, P. J., Plank, T., Edmonds, M. and Hauri, E. H., 2015. Volatiles in Magmas. In: Sigurdsson H., Houghton B., McNutt S.R., Rymer H., Stix J. (Eds.). The encyclopedia of volcanoes, second edition, 163 – 183. http://dx.doi.org/10.1016/B978-0-12-385938-9.00007-9.

Watson, E. B. and Liang, Y., 1995. A simple model for sector zoning in slowly-grown crystals: implications for growth rate and lattice diffusion, with emphasis on accessory minerals in crustal rocks. American Mineralogist, 80, 1170–1182.

Wilding, M. C., Webb, S. L. and Dingwell, D. B., 1995. Evaluation of a relaxation geospeedometer for volcanic glasses. Chemical Geology, 125, 137 – 148.

Wohletz, K., Civetta, L. and Orsi, G., 1999. Thermal evolution of the Phlegrean magmatic system. Journal of Geothermal Research, 91, 381–414.

Wood, B. J. and Blundy, J. D., 1997. A predictive model for rare earth element partitioning between clinopyroxene and anhydrous silicate melt. Contribution to Mineralogy and Petrology, 129, 166–181.

Wood, B. J., 1990. An experimental test of the spinel peridotite oxygen barometer. Journal of Geophysical Research-Solid Earth and Planets, 95(B10), 15845-15851.

Wood, B. J., Bryndzia, L. T. and Johnson, K. E., 1990. Mantle Oxidation-State and Its Relationship to Tectonic Environment and Fluid Speciation. Science, 248(4953), 337-345.

Zhang, W., Zeng, Z., Cui, L. and Yin, X., 2018. Geochemical constraints on MOBR composition and magma sources at East Pacific rise between 1°S and 2°S. J. Ocean. Univ. China (Oceanic and Coastal Sea Research), 17 (2), 297 – 304.

Zhang, Y., 2008. Geochemical Kinetic. Princeton University Press, New York.

Zhou, W., Van der Voo, R., Peacor, D. R. and Zhang, Y., 2000. Variable Ti-content and grain size of titanomagnetite as a function of cooling rate in very young MORB. Earth and Planetary Science Letters. 179, 9 – 20.

Figure 1a. Chemical variations of major oxides (wt.%) in spinel (sp) as a function of log (°C/h). Average data are listed in Tab. 3a. Only linear regressions with $R^2 \geq 0.8$ are plotted in the figure. The 95% confidence interval refers to the average chemical values measured for crystals solidified at different cooling rates. The yellow diamond is the virtual equilibrium compositions computed with alpha melts (Smith and Asimow, 2005; Ghiorso et al., 2002; Asimow and Ghiorso 1998), grey circles and star refer to Mollo et al., (2013) and, white (QFM), blue (QFM+1), purple (QFM+5) squares and purple star refer to Hammer (2006).

Figure 1b. Chemical variations of major oxides (wt.%) in clinopyroxene (cpx) as a function of log $\Delta T/\Delta t$ (°C/h). Average data are listed in Tab. 3b. Only linear regressions with $R^2 \geq 0.8$ are plotted in the figure. The 95% confidence interval refers to the average chemical values measured for crystals solidified at different cooling rates. The yellow and yellow and black diamonds are the

virtual equilibrium compositions computed with alpha melts (Smith and Asimow, 2005; Ghiorso et al., 2002; Asimow and Ghiorso 1998), white triangles and star refer to and Baker and Grove (1985), black circles and star refer to Schiffmann and Lofgren (1982), grey circles and star refer to Mollo et al., (2010) and green (QFM-3.6), white (QFM), blue (QFM+1), purple (QFM+5) squares and purple star refer to Hammer (2006).

Figure 1c. Chemical variations of major oxides (wt.%) in plagioclase (plg) as a function of log $\Delta T/\Delta t$ (°C/h); average data in Tab. 3c. Only linear regressions with $R^2 \geq 0.8$ are plotted in the figure. The 95% confidence interval refers to the average chemical values measured for crystals solidified at different cooling rates. The yellow diamond is the virtual equilibrium compositions computed with alpha melts (Smith and Asimow, 2005; Ghiorso et al., 2002; Asimow and Ghiorso 1998), white triangles and star refer to and Baker and Grove (1985), black circles and star refer to Schiffmann and Lofgreen (1982), grey circles and star refer to Mollo et al., (2011).

Figure 1d. Chemical variations of major oxides (wt.%) in the glass as a function of log $\Delta T/\Delta t$ (°C/h). Average data are listed in Tab. 3d. White triangles and star refer to and Baker and Grove (1985), black circles and star refer to Schiffmann and Lofgren (1982), grey circles and star refer to Mollo et al., (2011b) and green (QFM-3.6), white (QFM), blue (QFM+1), purple (QFM+5) squares and purple star refer to Hammer (2006).

Figure 2. Cation variations in clinopyroxene (cpx) as a function of $\Delta T/\Delta t$. All data are expressed as atom per formula unit (a.p.f.u.). Only linear regressions with $R^2 \geq 0.8$ are plotted in the figure with confident intervals at 95%.

Figure 3. Relationships between the most abundant components (≥ 10 mol.%) in cpx (left) and their ratio *versus* $\Delta T/\Delta t$ (right). The solid black lines are the linear regressions, while the dashed red ones are the 95% confidence ranges; data are listed in Table 3Sb.

Figure 4a. Maximum and average growth rates (G_{max} and G_{CSD}) (cm/s) *versus* TiO_2 + Fe_2O_3 (wt.%) + Sp*s.s.* (mol.%) measured in sp. Data are listed in Tabs. 3a, 3Sa and 4. Only linear regressions with $R^2 \geq 0.8$ are plotted in the figure with confident intervals at 95%. The x-axis is represented in log-scale.

Figure 4b. Maximum and average growth rates (G_{max} and G_{CSD}) (cm/s) *versus* Al_2O_3 + Fe_2O_3 + MgO + CaO + Na_2O (wt.%) measured in cpx. Data are listed in Tabs. 3b and 4. Only linear regressions with $R^2 \geq 0.8$ are plotted in the figure with confident intervals at 95%. The x-axis is represented in log-scale.

Figure 4c. Maximum and average growth rates (G_{max} and G_{CSD}) (cm/s) *versus* Di + En + Fs + Hd + Jd + CaTs + CaFeTs (mol.%) measured in cpx. Data are listed in Tabs. 3b, 3Sb and 4. Only linear regressions with $R^2 \geq 0.8$ are plotted in the figure with confident intervals at 95%. The x-axis is represented in log-scale.

Figure 4d. Maximum and average growth rates (G_{max} and G_{CSD}) (cm/s) *versus* Al_2O_3 + Fe_2O_3 + MgO + Na_2O (wt.%) + An + Ab (mol.%) measured in plg. Data are listed in Tabs. 3c, 3Sc and 4. Only linear regressions with $R^2 \geq 0.8$ are plotted in the figure with confident intervals at 95%. The x-axis is represented in log-scale.

Figure 5a. Note: Oxygen fugacity across tectonic setting. Redrawn after Cottrell et al., (2021).

Figure 5b. Experimental conditions for oxygen fugacity reported as ΔQFM (where QFM refers to the Quartz-Fayalite-Magnetite buffer) for Hammer (2006; H2006), Baker and Grove (1985; B&G1995), Schiffmann and Lofgreen (1982; S&L1982) and Mollo et al., (2010, 2011b, 2013b; M2011). Crosses symbols refer to calculated oxygen fugacity using the Kress and Carmichael (1991) model at temperature of 1600, 1300 and 1218 °C (the liquidus temperature for our starting material estimated by using the alphaMELTS 1.9 code (see text for details).

Figure 6. Test for the *equilibrium* crystallization of cpx and plg as a function of cooling rate ($\Delta T/\Delta t$). $^{cpx\text{-}melt}Kd_{Fe\text{-}Mg}$ and $^{plg\text{-}melt}Kd_{An\text{-}Ab}$ were obtained using the models of Putirka et al. (1996) and Putirka et al. (2008), respectively. The crystallization temperatures were calculated using the models of Putirka et al. (2008) for both cpx and plg.

Figure 7. Hypothetical solidification sketch of a MORB lava with a thickness of 0.5 m (top) and 1.5 m (bottom). $\Delta T/\Delta t$(°C/h) and textural parameters are those measured by Giuliani et al. (2020a, 2020b). Qualitative textures on the right side of the figure are modified from the experiments of Vetere et al. (2013, 2015).

Table 1. Average chemical compositions of the starting material (B_{100}) used in this study and the synthetic trachybasalt investigated in Mollo et al. (2010; 2011b; 2013b), the high-Fe basalt used in Hammer (2006), a basaltic andesite in Baker and Grove (1985) and an evolved pillow basalt in Schiffman and Lofgren (1982).

oxide (wt.%)	EPMA	SEM	|Δ|[a]	M2013	H2006	B&G1985	S&L1982
SiO_2	47.3 (0.5)	46.5 (0.5)	0.7	47.6	51.40	54.00	53.64
TiO_2	1.0 (0.0)	0.9 (0.2)	0	1.6	1.63	0.95	1.85
Al_2O_3	15.4 (0.1)	16.0 (0.5)	0.6	16.8	9.13	17.90	14.08
FeO	10.2 (0.0)	11.2 (0.8)	1	10.6	13.90	7.68	11.80
Fe_2O_3	11.3 (0.0)	12.4 (0.8)	1.1	11.8	-	-	-
MnO	0.2 (0.1)	0.0 (0.0)	0.2	0.2	-	0.14	0.19
MgO	9.4 (0.2)	9.4 (0.3)	0	6.5	7.27	5.87	4.89
CaO	12.8 (0.2)	12.5 (0.5)	0.3	11.1	8.77	8.73	8.02
Na_2O	1.9 (0.1)	1.9 (0.5)	0.1	3.3	2.13	3.29	3.08
K_2O	0.1 (0.0)	0.2 (0.1)	0.1	1.8	0.49	0.97	1.16
P_2O_5	-	0.1 (0.2)	-	0.5	-	-	-
Total (FeO)	98.0 (0.7)	98.6 (0.2)	0.7	98.2	99.72	99.53	98.71
Total (Fe_2O_3)	99.1 (0.7)	99.8 (0.2)	0.8	99.1	101.82	100.38	100.02
H_2O (ppm)[b]		53					
Fe^{2+}/Fe_{tot} [c]		0.886					

Footnotes: [a]|Δ| = difference between oxide wt.% by EPMA-WDS and oxide wt.% by SEM-EDS. The standard deviations are reported in parentheses. [b]H_2O and [c]Fe^{2+}/Fe_{tot} ratio for B_{100} were estimated by FTIR spectroscopy and the modified Wilson's method respectively, as reported in Vetere et al., (2013, 2015). Note that Fe is reported as both Fe^{2+} and Fe^{3+}. The B_{100} bulk composition corresponds to basalt in the TAS diagram (Le Maitre, 2002).

Table 2. Conditions of dynamic cooling experiments run by Vetere et al. (2013, 2015).

label	heating rate (°C/h)	T_i (°C)	dwell time (h)	ΔT/Δt (°C/h)	T_f (°C)	experimental time (h)
E1b	420	1300	2	1	800	510.7
E1a				1		510.7
E7				7		72.6
E60				60		13.4
E180a		1400°C for 0.5h 1300°C for 40h		180		47.8
E180b		1300	2	180		8.8
E1800				1800		5.3
E9000				9000		5.1
E-quench				≥ 10^5	1300	3.2

Footnoted: T_i and T_f refer to the initial and final temperatures of the experiments.

Table 3a. Average compositions in wt% of sp determined by EPMA-WDS and SEM-EDS (*).

ÄT/Ät(°C/h)	1	7	60	180
label	E1b	E7	E60	E180b
# analytical points	16	54	18 + 9*	15
SiO_2	0.1 (0.0)	0.1 (0.0)	0.2 (0.2)	0.2 (0.0)
TiO_2	1.4 (0.3)	1.4 (0.7)	1.0 (0.3)	0.6 (0.1)
Al_2O_3	7.1 (0.1)	10.0 (3.8)	14.2 (1.4)	14.0 (0.5)
FeO	66.6 (0.2)	64.6 (2.3)	64.2 (3.2)	60.4 (0.9)
Fe_2O_3	74.0 (0.2)	71.8 (2.6)	71.3 (3.5)	67.1 (1.0)
MnO	0.8 (0.2)	0.6 (0.3)	0.2 (0.2)	0.4 (0.1)
MgO	16.2 (0.7)	17.0 (0.3)	12.9 (1.2)	18.5 (0.6)
CaO	0.1 (0.1)	0.1 (0.1)	0.3 (0.1)	0.2 (0.1)
Na_2O	0.0 (0.0)	0.0 (0.0)	0.1 (0.2)	0.2 (0.2)
Total (FeO)	92.6 (0.6)	93.9 (0.7)	93.3 (1.7)	94.4 (0.3)
Total (Fe_2O_3)	99.8 (0.3)	101.1 (0.5)	100.4 (2.0)	101.1 (0.3)

Footnote: sp chemical data selected by considering oxide totals between 97 and 103 wt.%. The standard deviations are reported in parenthesis.

Table 3b. Average compositions in wt.%, of cpx determined by EPMA-WDS.

ÄT/Ät(°C/h)	1	7	60	180	1800
label	E1b	E7	E60	E180b	E1800
# analytical points	62	80	59	56	57
SiO_2	48.0 (1.6)	45.8 (1.7)	45.7 (0.8)	45.1 (1.5)	46.4 (1.3)
TiO_2	0.8 (0.2)	1.0 (0.2)	0.9 (0.1)	0.8 (0.1)	0.9 (0.1)
Al_2O_3	6.0 (1.1)	7.4 (1.0)	10.6 (0.5)	12.5 (1.4)	13.8 (1.4)
FeO	8.1 (0.9)	9.7 (1.2)	8.6 (0.6)	10.3 (0.8)	10.5 (1.2)
Fe_2O_3	9.0 (1.0)	10.8 (1.3)	9.6 (0.6)	11.4 (0.9)	11.6 (1.3)
MnO	0.2 (0.1)	0.2 (0.1)	0.1 (0.0)	0.2 (0.1)	0.2 (0.0)
MgO	16.8 (1.7)	14.8 (1.4)	14.3 (1.1)	12.7 (1.5)	12.6 (1.7)
CaO	18.6 (1.3)	18.9 (1.2)	19.4 (1.2)	16.7 (1.0)	14.6 (1.2)
Na_2O	0.4 (0.1)	0.6 (0.2)	0.3 (0.1)	0.8 (0.3)	0.8 (0.3)
Total (FeO)	99.0 (0.7)	98.4 (0.6)	99.9 (0.6)	99.2 (0.6)	99.8 (0.7)
Total (Fe_2O_3)	99.9 (0.7)	99.5 (0.5)	100.8 (0.6)	100.3 (0.6)	101.0 (0.7)

Footnote: cpx chemical data selected by considering oxide totals between 99 and 101 wt.%. The standard deviationsare in parenthesis.

Table 3c. Average compositions in wt.% of plg determined by EPMA-WDS and SEM-EDS (*).

ÄT/Ät(°C/h)	1	7	60
label	E1b	E7	E60
# analytical points	194	118	27*
SiO_2	49.8 (2.3)	49.8 (1.2)	51.6 (1.2)

TiO_2	0.1 (0.1)	0.1 (0.1)	0.2 (0.2)
Al_2O_3	29.8 (1.7)	29.0 (0.9)	25.9 (1.1)
FeO	2.5 (0.2)	3.0 (0.3)	3.7 (0.8)
Fe_2O_3*	2.8 (0.2)	3.3 (0.3)	4.1 (0.9)
MnO	0.0 (0.0)	0.0 (0.0)	0.1 (0.1)
MgO	0.4 (0.2)	0.5 (0.2)	1.5 (0.8)
CaO	14.3 (1.8)	14.3 (1.1)	13.1 (0.8)
Na_2O	3.1 (1.1)	3.4 (0.7)	3.3 (0.4)
Total (FeO)	100.0 (0.7)	100.1 (0.6)	99.7 (0.8)
Total (Fe_2O_3)	100.2 (0.7)	100.4 (0.6)	100.1 (0.7)

Footnote: plg chemical data selected by considering totals between 99 and 101 wt.%. The standard deviations are in parenthesis.

Table 3d. Average compositions in wt.% of glass determined by EPMA-WDS and SEM-EDS (*).

ÄT/Ät(°C/h)	180	1800		9000
label	E180b	E1800		E9000
	intra	intra	matrix	matrix
# analytical points	12+1*	22	16+6*	309
SiO_2	58.9 (2.1)	54.1 (1.5)	47.9 (0.7)	48.3 (0.4)
TiO_2	0.8 (0.1)	0.9 (0.1)	0.9 (0.2)	0.9 (0.1)
Al_2O_3	20.1 (0.9)	21.9 (1.3)	16.0 (0.2)	16.0 (0.2)
FeO	3.3 (0.5)	6.7 (1.3)	10.5 (0.8)	9.8 (0.3)
Fe_2O_3	4.3 (0.8)	7.4 (1.4)	11.6 (0.9)	10.9 (0.3)
MnO	0.1 (0.1)	0.1 (0.0)	0.1 (0.1)	0.2 (0.0)
MgO	3.9 (0.8)	3.7 (1.0)	9.5 (0.2)	9.4 (0.2)
CaO	8.3 (1.1)	8.9 (1.4)	12.9 (0.4)	12.8 (0.2)
Na_2O	3.6 (0.4)	3.7 (0.5)	1.5 (0.3)	2.0 (0.2)
Total (FeO)	99.8 (0.7)	100.1 (0.9)	99.4 (0.7)	99.5 (0.5)
Total (Fe_2O_3)	100.2 (0.7)	100.9 (1.0)	100.5 (0.6)	100.5 (0.5)

Footnote: "intra" and "matrix" correspond to the glass analyzed at a distance ≤ and > 50 μm from the crystal rims, respectively. Chemical data selected by considering totals between 99 and 101 wt.% The standard deviation is in parenthesis.

Table 4. Textural attributes of sp, cpx, plg, and glass from Giuliani et al. (2020b).

label	$\Delta T/\Delta t$ (°C/h)	crystalline phase	mass balance (wt.%)	area%	L_{max} (μm)	G_{max} (cm/s)	G_{CSD} (cm/s)	crystal shape
E1b	1	plg	42.5	65.6 (6.6)	949	$4.7*10^{-8}$	$6.4*10^{-9}$	
		cpx	51.2	30.6 (5.6)	398	$1.9*10^{-8}$	$2.1*10^{-9}$	
		sp	6.3	3.4 (0.9)	98	$5.1*10^{-9}$	$2.1*10^{-9}$	
		crystals	57.5	99.6 (0.8)		-		
		glass	-	1.9 (0.0)				
E7	7	plg	40.5	60.7 (4.3)	751	$2.4*10^{-7}$	$4.5*10^{-8}$	faceted
		cpx	55.2	36.0 (4.5)	264	$1.0*10^{-7}$	$1.1*10^{-8}$	
		sp	4.3	3.3 (0.4)	76	$2.8*10^{-8}$	$3.4*10^{-9}$	
		crystals	59.5	100.0 (0.0)		-		
		glass	-	-				
E60	60	plg	45.6	46.1 (2.3)	109	$3.5*10^{-7}$	$4.3*10^{-8}$	

		cpx	48.9	47.0 (3.2)	104	$2.7*10^{-7}$	$3.2*10^{-8}$	
		sp	5.5	4.5 (0.6)	20	$6.4*10^{-8}$	$1.1*10^{-8}$	
		crystals	54.4	97.6 (0.8)		-		
		glass	-	2.4 (0.8)				
E180b	180	cpx	58.5	50.6 (1.5)	104	$1.0*10^{-6}$	$1.4*10^{-7}$	
		sp	4.7	4.6 (0.8)	65	$6.3*10^{-7}$	$7.2*10^{-8}$	
		crystals	63.2	55.3 (1.1)		-		
		glass	36.8	44.7 (1.1)				
E1800	1800	cpx	58.7	51.0 (1.3)	25	$2.5*10^{-6}$	$2.7*10^{-7}$	dendritic
		sp	-	1.2 (0.0)	6	$6.2*10^{-7}$	$6.8*10^{-8}$	
		crystals	58.7	52.2 (1.3)	-			
		glass	41.3	47.9 (1.3)				
E9000	9000	cpx+sp		1.8 (0.8)	7	-		
		crystals	-	1.8 (0.8)	-			
		glass		98.3 (0.7)				

Footnotes: G_{max}(cm/s) is the maximum growth rate and has been computed by considering the ratio between the average lengths of the five longest crystals and the experimental time (*t* from T_{n} to quench temperature). G_{CSD} (cm/s) is the average growth rate and has been obtained following Zieg and Marsh (2002) as -1/*mt*, where *m* is the CSD slope and *t* the experimental time. Both the CSD parameters (*m* and n_0) are referred to the full-size range of the CSD curve so that they represent average values.

Highlights:

- Dynamic solidification of a MORB liquid from 1 to 9000 °C/h
- Sp, cpx, and plg chemical changes as a function of cooling rate
- (*Dis*)*equilibrium* kinetics of crystallization provides geospeedometers
- Order of mineral segregation
- Crystal-chemical and textural variations are quantitatively related

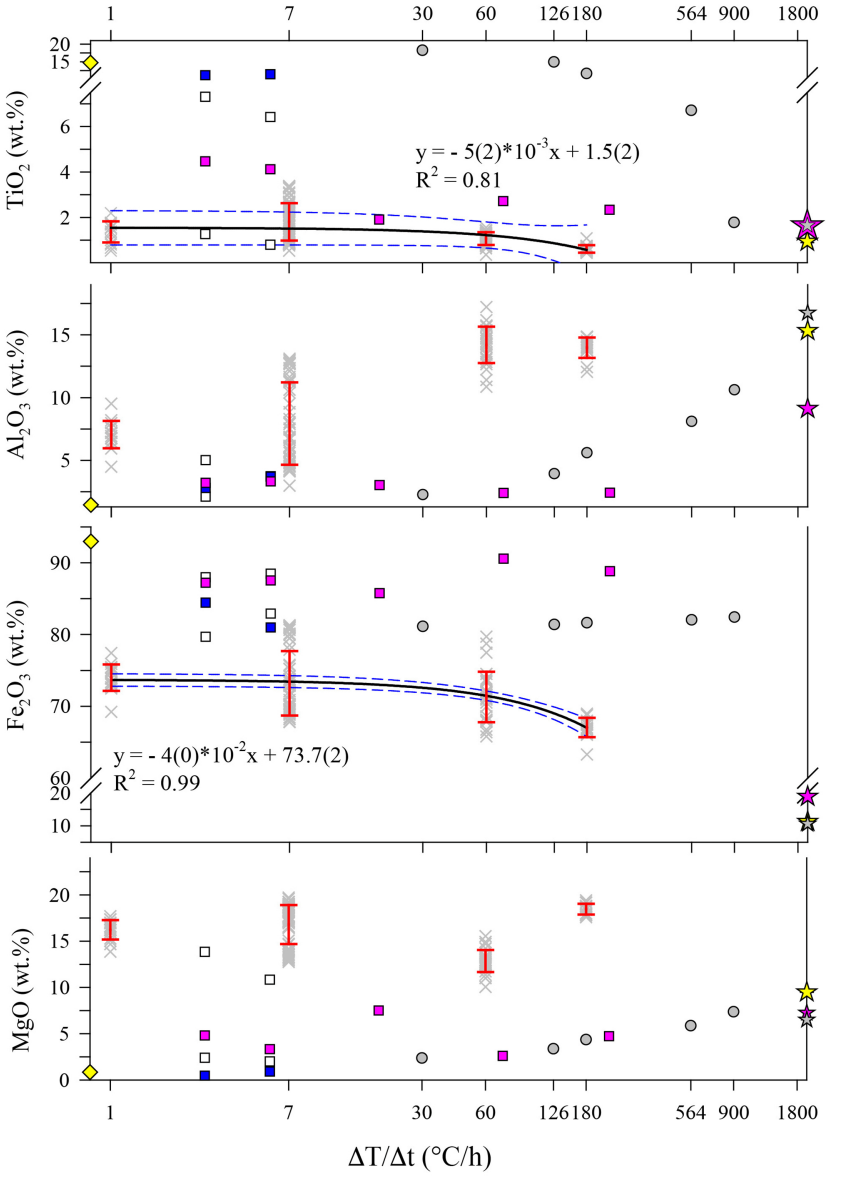
TiO2 (wt.%)
y = - 5(2)*10-3x + 1.5(2)
R2 = 0.81
Al2O3 (wt.%)
Fe2O3 (wt.%)
y = - 4(0)*10-2x + 73.7(2)
R2 = 0.99
MgO (wt.%)
1
7
30
60
126
180
564
900
1800
ΔT/Δt (°C/h)
This work-starting composition
H2006-starting material
M2013b-Starting material
Sp (alphamelts)
linear regression
This work-single point
M2013b QFM+2.2
H2006 QFM
H2006 QFM+1
H2006 QFM+5
95% Confidence Band

Figure 1A

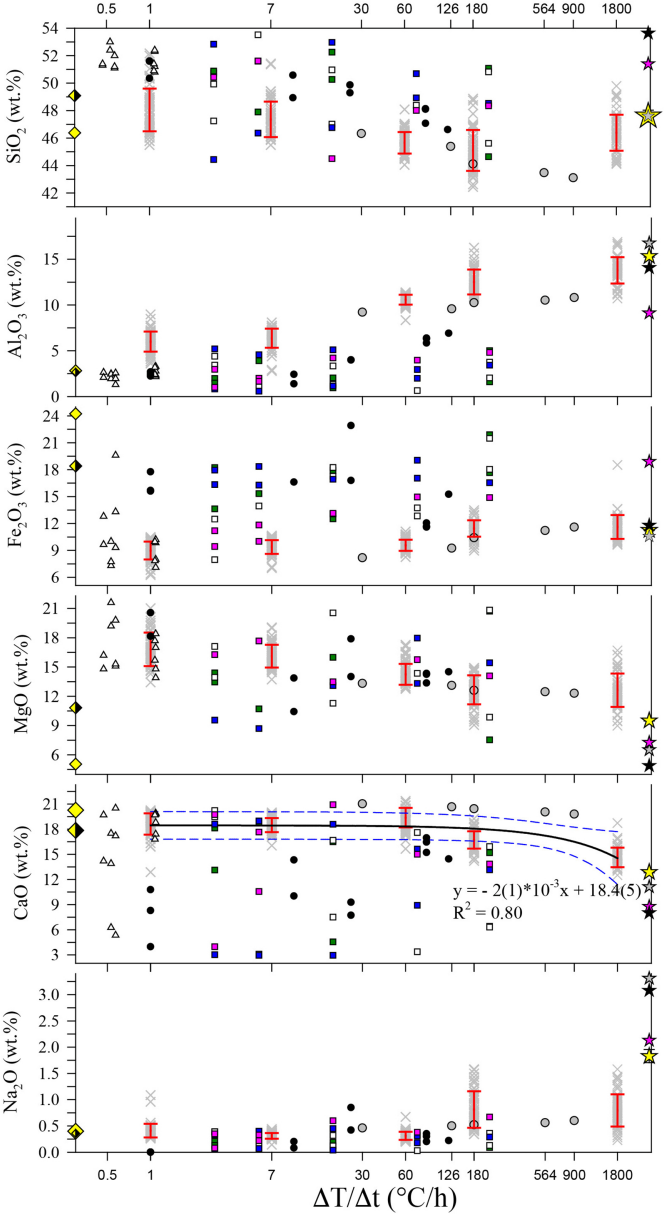
0.5
1
7
30
60
126
180
564
900
1800
SiO2 (wt.%)
Al2O3 (wt.%)
Fe2O3 (wt.%)
MgO (wt.%)
CaO (wt.%)
Na2O (wt.%)
y = - 2(1)*10-3x + 18.4(5)
R2 = 0.80
ΔT/Δt (°C/h)
This work-starting composition
H2006-starting material
M2010-Starting material
B&G1985-starting maerial
S&L1982-starting maerial
This work-single point
M2010 QFM+ 2.2
B&G1985 QFM
S&L1982 QFM
linear regression
95% Confidence Band
H2006 QFM+5
H2006 QFM+1
H2006 QFM
H2006 QFM-4
Px 1 and 2
(alphamelts)

Figure 1B

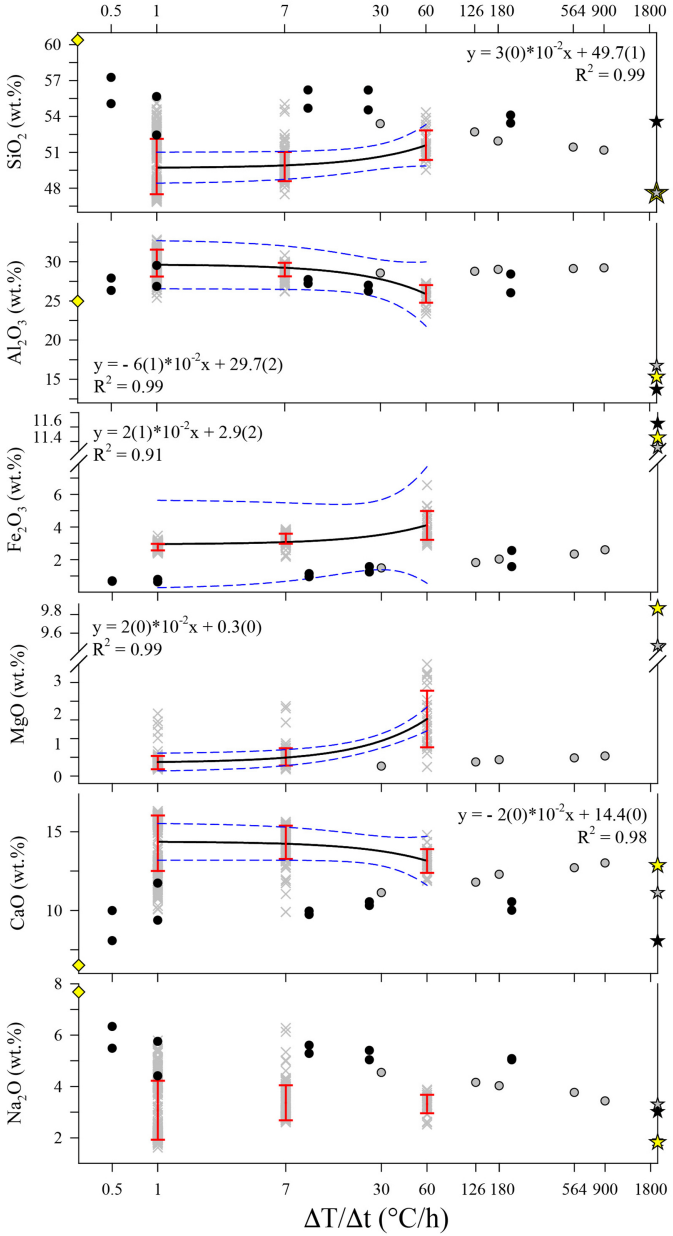
0.5
1
7
30
60
126
180
564
900
1800
SiO2 (wt.%)
y = 3(0)*10-2x + 49.7(1)
R2 = 0.99
Al2O3 (wt.%)
y = - 6(1)*10-2x + 29.7(2)
R2 = 0.99
Fe2O3 (wt.%)
y = 2(1)*10-2x + 2.9(2)
R2 = 0.91
MgO (wt.%)
y = 2(0)*10-2x + 0.3(0)
R2 = 0.99
CaO (wt.%)
y = - 2(0)*10-2x + 14.4(0)
R2 = 0.98
Na2O (wt.%)
ΔT/Δt (°C/h)
This work-starting composition
M2011b-Starting material
S&L1982-starting maerial
This work-single point
M2011b QFM+2.2
B&G1985 QFM
S&L1982 QFM
Plg (alphamelts)
linear regression
95% Confidence Band

Figure 1C

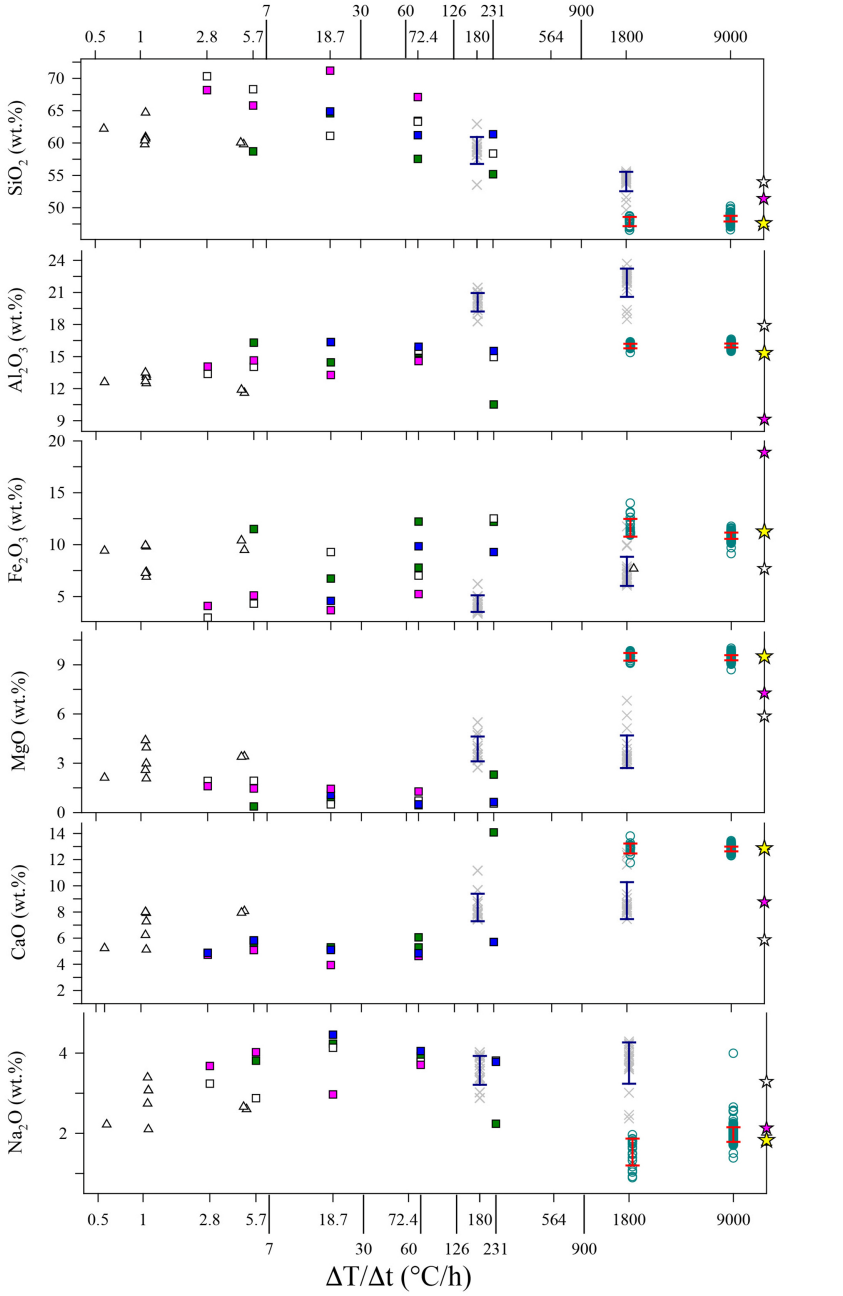
0.5
1
2.8
5.7
7
18.7
30
60
72.4
126
180
231
564
900
1800
9000
SiO2 (wt.%)
Al2O3 (wt.%)
Fe2O3 (wt.%)
MgO (wt.%)
CaO (wt.%)
Na2O (wt.%)
ΔT/Δt (°C/h)
This work-starting composition
H2006-starting material
M2011b-Starting material
B&G1985-starting maerial
linear regression
This work single point matrix glass
This work-single point
M2011b QFM + 2.2
B&G1985 QFM
95% Confidence Band
H2006 QFM+5
H2006 QFM+1
H2006 QFM
H2006 QFM-4

Figure 1D

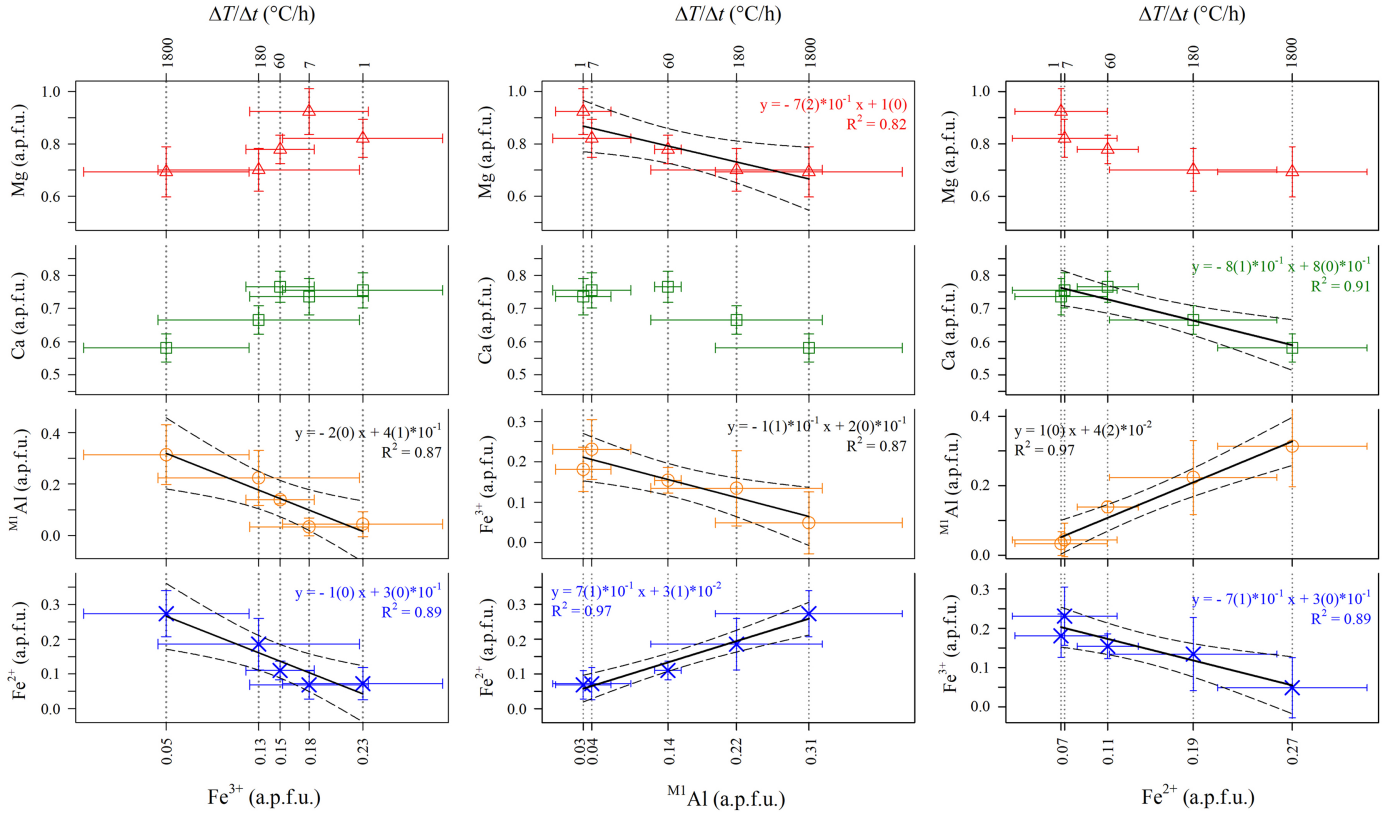
ΔT/Δt (°C/h)
1800
180
60
7
1
Mg (a.p.f.u.)
Ca (a.p.f.u.)
M1 Al (a.p.f.u.)
Fe2+ (a.p.f.u.)
y = - 2(0) x + 4(1)*10-1
R2 = 0.87
y = - 1(0) x + 3(0)*10-1
R2 = 0.89
0.05
0.13
0.15
0.18
0.23
Fe3+ (a.p.f.u.)
ΔT/Δt (°C/h)
1
7
60
180
1800
y = - 7(2)*10-1 x + 1(0)
R2 = 0.82
y = - 1(1)*10-1 x + 2(0)*10-1
R2 = 0.87
y = 7(1)*10-1 x + 3(1)*10-2
R2 = 0.97
0.03
0.04
0.14
0.22
0.31
M1Al (a.p.f.u.)
ΔT/Δt (°C/h)
1
7
60
180
1800
y = - 8(1)*10-1 x + 8(0)*10-1
R2 = 0.91
y = 1(0) x + 4(2)*10-2
R2 = 0.97
y = - 7(1)*10-1 x + 3(0)*10-1
R2 = 0.89
0.07
0.11
0.19
0.27
Fe2+ (a.p.f.u.)

Figure 2

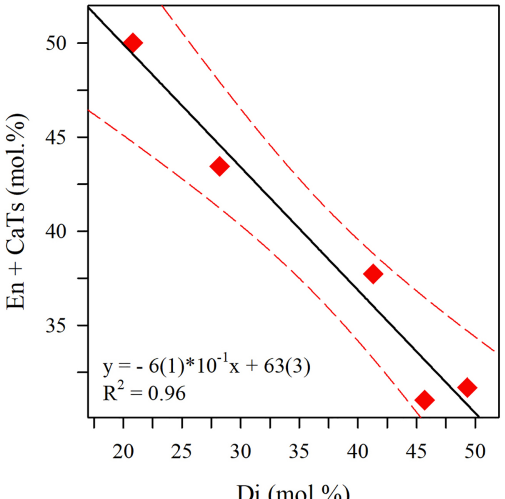
En + CaTs (mol.%)
50
45
40
35
y = - 6(1)*10-1x + 63(3)
R2 = 0.96
20
25
30
35
40
45
50
Di (mol.%)

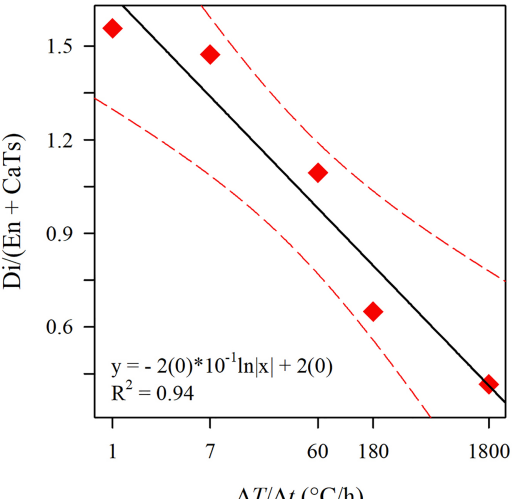
Di/(En + CaTs)
1.5
1.2
0.9
0.6
y = - 2(0)*10-1ln|x| + 2(0)
R2 = 0.94
1
7
60
180
1800
ΔT/Δt (°C/h)

Figure 3

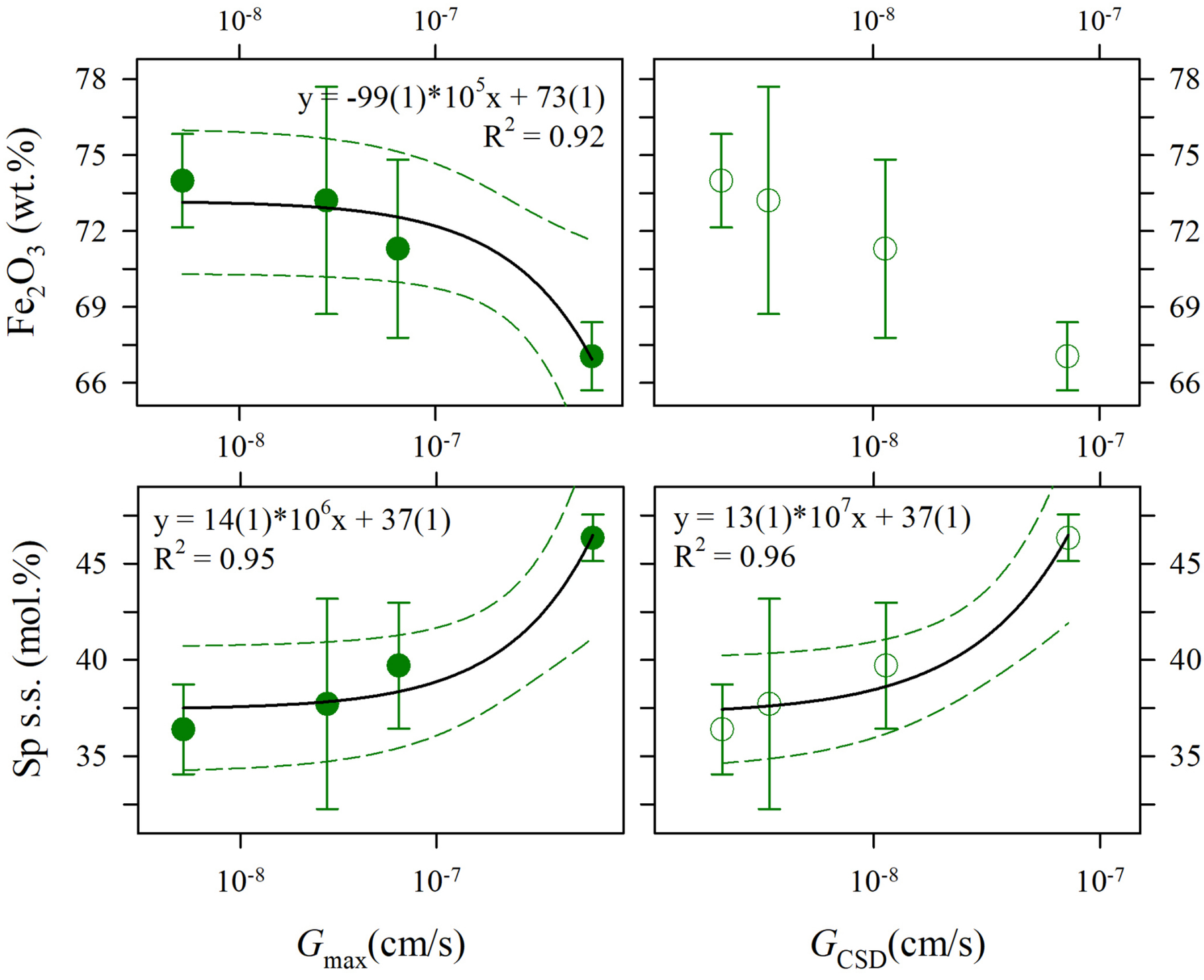
y = -99(1)*10^5x + 73(1)
R^2 = 0.92
y = 14(1)*10^6x + 37(1)
R^2 = 0.95
y = 13(1)*10^7x + 37(1)
R^2 = 0.96
Fe2O3 (wt.%)
Sp s.s. (mol.%)
G_max(cm/s)
G_CSD(cm/s)
10^-8
10^-7
78
75
72
69
66
45
40
35

Figure 4A

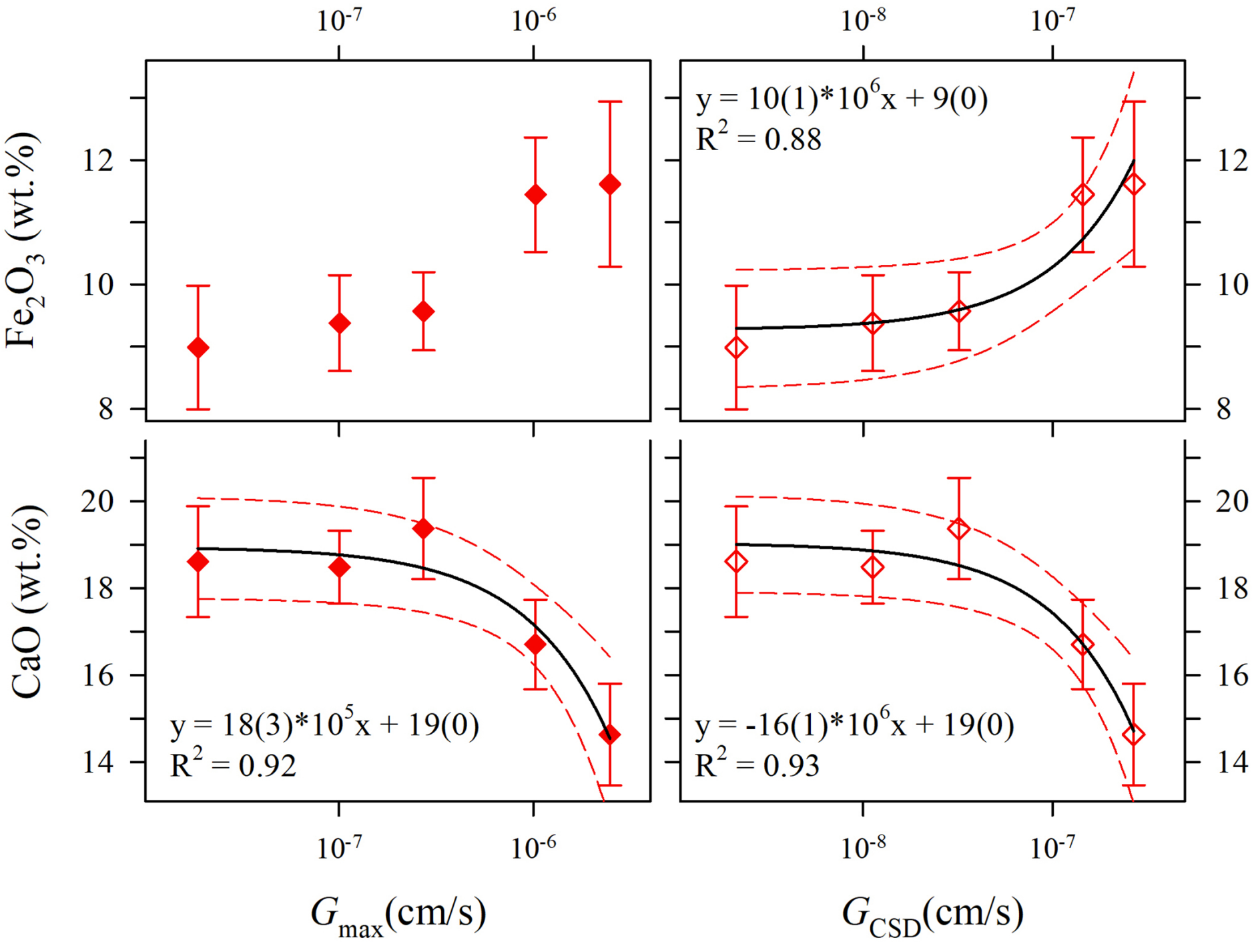
10-7
10-6
10-8
10-7
Fe2O3 (wt.%)
12
10
8
y = 10(1)*10^6x + 9(0)
R^2 = 0.88
CaO (wt.%)
20
18
16
14
y = 18(3)*10^5x + 19(0)
R^2 = 0.92
y = -16(1)*10^6x + 19(0)
R^2 = 0.93
Gmax(cm/s)
GCSD(cm/s)

Figure 4B

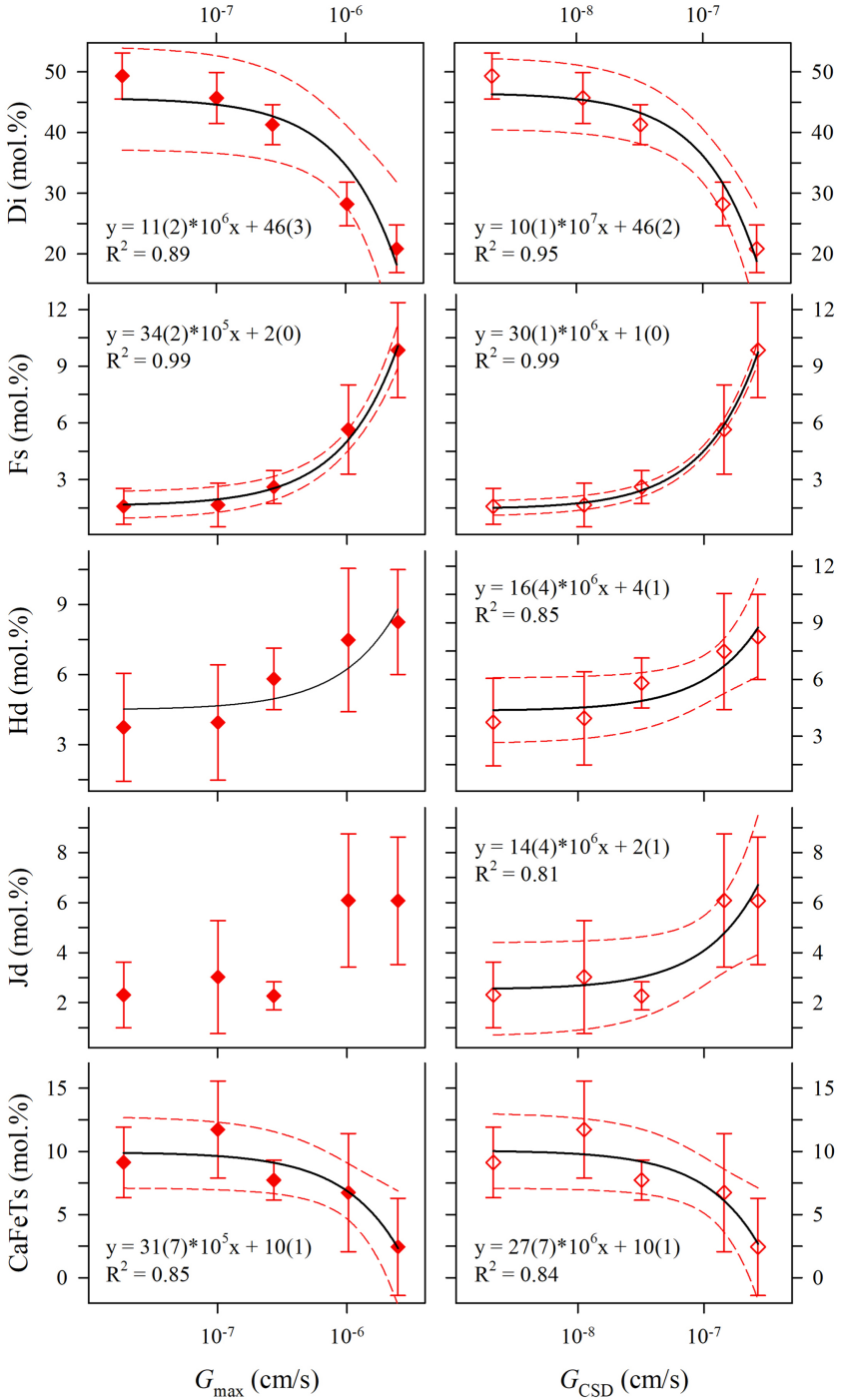
Di (mol.%)
y = 11(2)*10^6x + 46(3)
R^2 = 0.89
y = 10(1)*10^7x + 46(2)
R^2 = 0.95
Fs (mol.%)
y = 34(2)*10^5x + 2(0)
R^2 = 0.99
y = 30(1)*10^6x + 1(0)
R^2 = 0.99
Hd (mol.%)
y = 16(4)*10^6x + 4(1)
R^2 = 0.85
Jd (mol.%)
y = 14(4)*10^6x + 2(1)
R^2 = 0.81
CaFeTs (mol.%)
y = 31(7)*10^5x + 10(1)
R^2 = 0.85
y = 27(7)*10^6x + 10(1)
R^2 = 0.84
G_max (cm/s)
G_CSD (cm/s)

Figure 4C

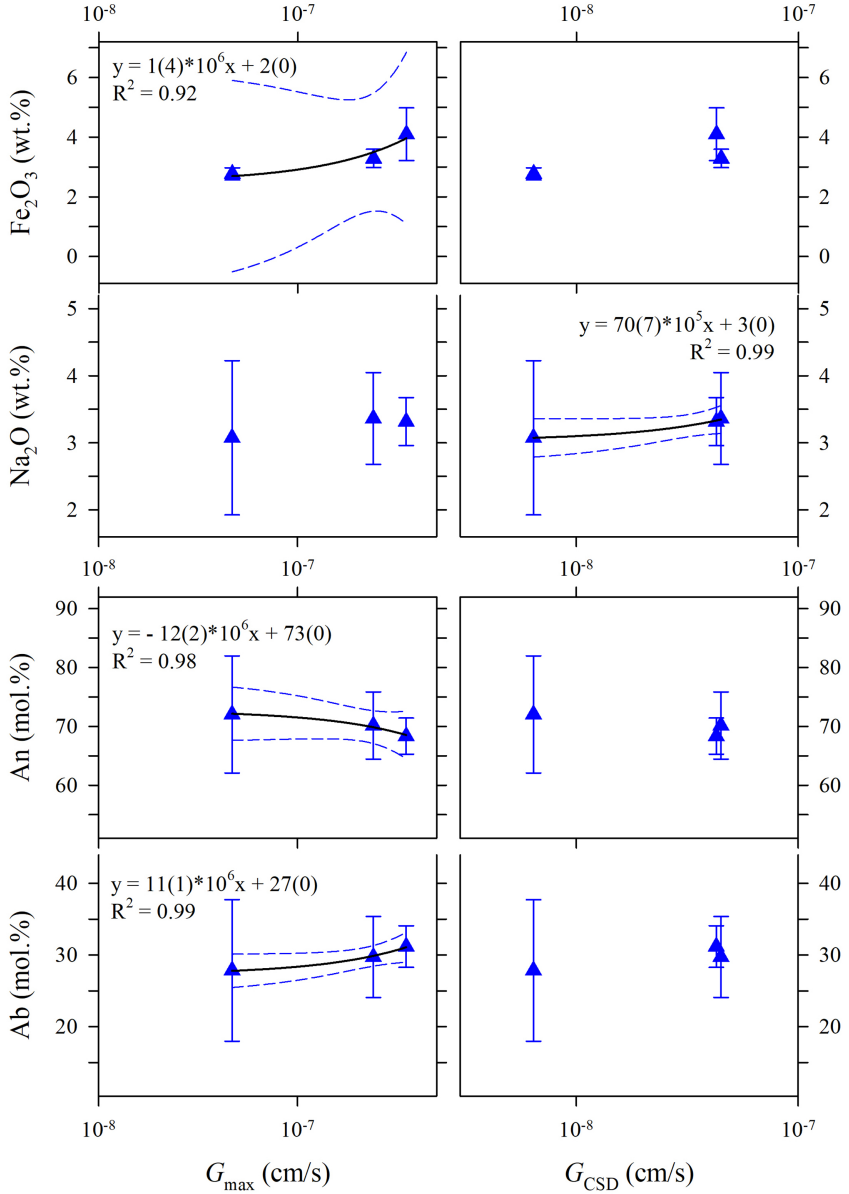
y = 1(4)*10^6x + 2(0)
R^2 = 0.92
Fe2O3 (wt.%)
y = 70(7)*10^5x + 3(0)
R^2 = 0.99
Na2O (wt.%)
y = - 12(2)*10^6x + 73(0)
R^2 = 0.98
An (mol.%)
y = 11(1)*10^6x + 27(0)
R^2 = 0.99
Ab (mol.%)
10^-8
10^-7
G_max (cm/s)
G_CSD (cm/s)

Figure 4D

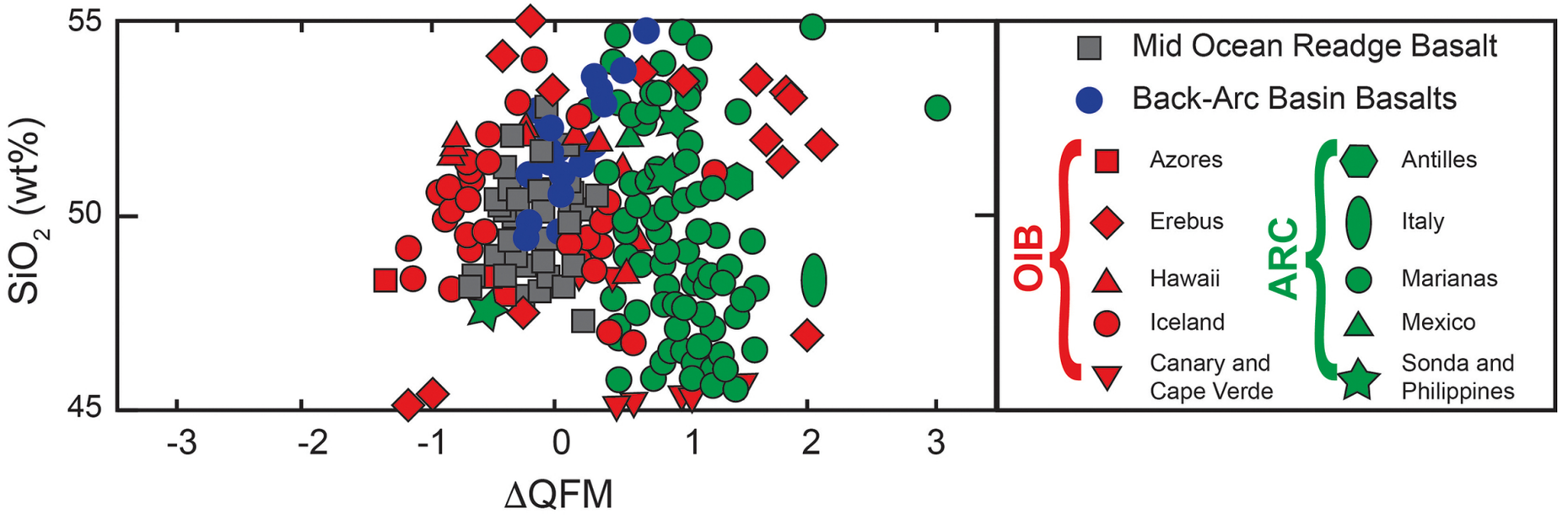
55
50
45
SiO2 (wt%)
-3
-2
-1
0
1
2
3
ΔQFM
Mid Ocean Readge Basalt
Back-Arc Basin Basalts
OIB
Azores
Erebus
Hawaii
Iceland
Canary and Cape Verde
ARC
Antilles
Italy
Marianas
Mexico
Sonda and Philippines

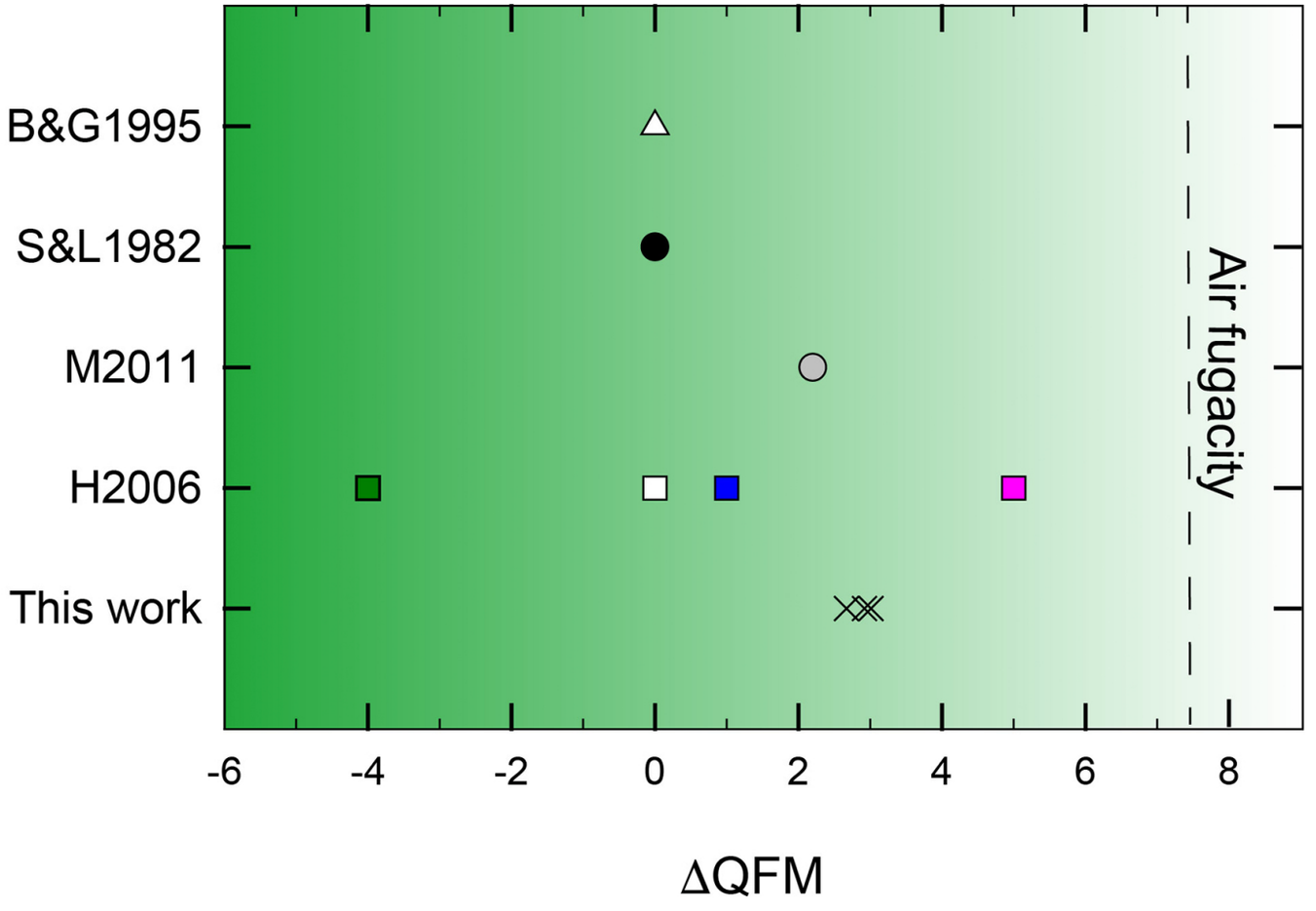
B&G1995
S&L1982
M2011
H2006
This work
Air fugacity
-6
-4
-2
0
2
4
6
8
ΔQFM

Figure 5

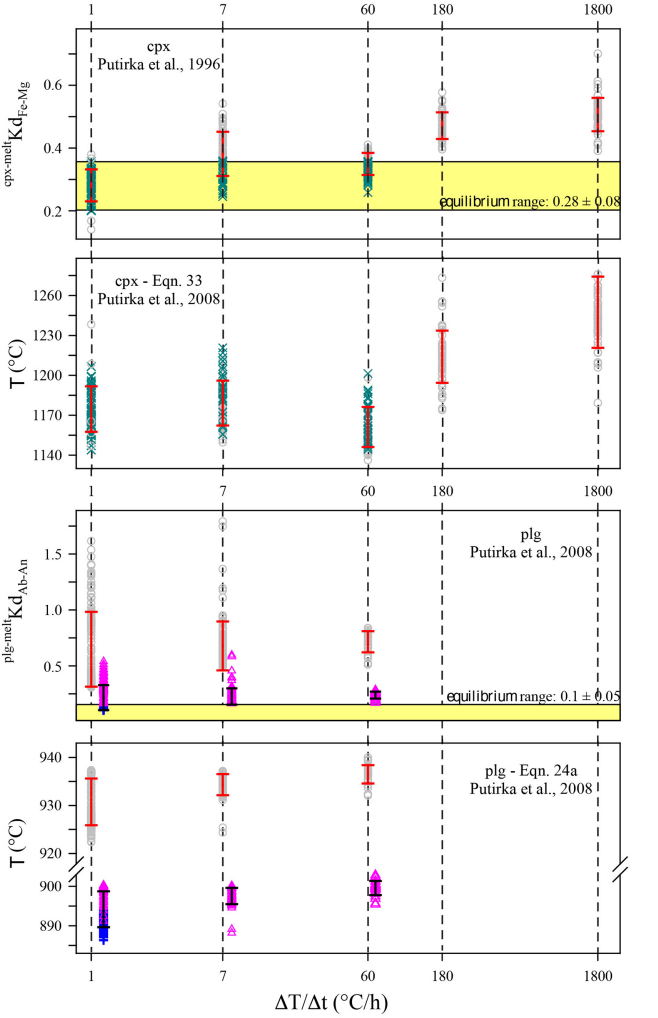

- bulk *versus* crystals core (equilibrium)
- intra-glass at 180 °C/h *versus* crystals core (equilibrium)
- intra-glass at 180 °C/h *versus* crystals core (disequilibrium)
- bulk *versus* crystals core (disequilibrium)
- standard deviation from bulck *versus* crystals core
- standard deviation from intra-glass at 180 °C/h *versus* crystals core

Figure 6

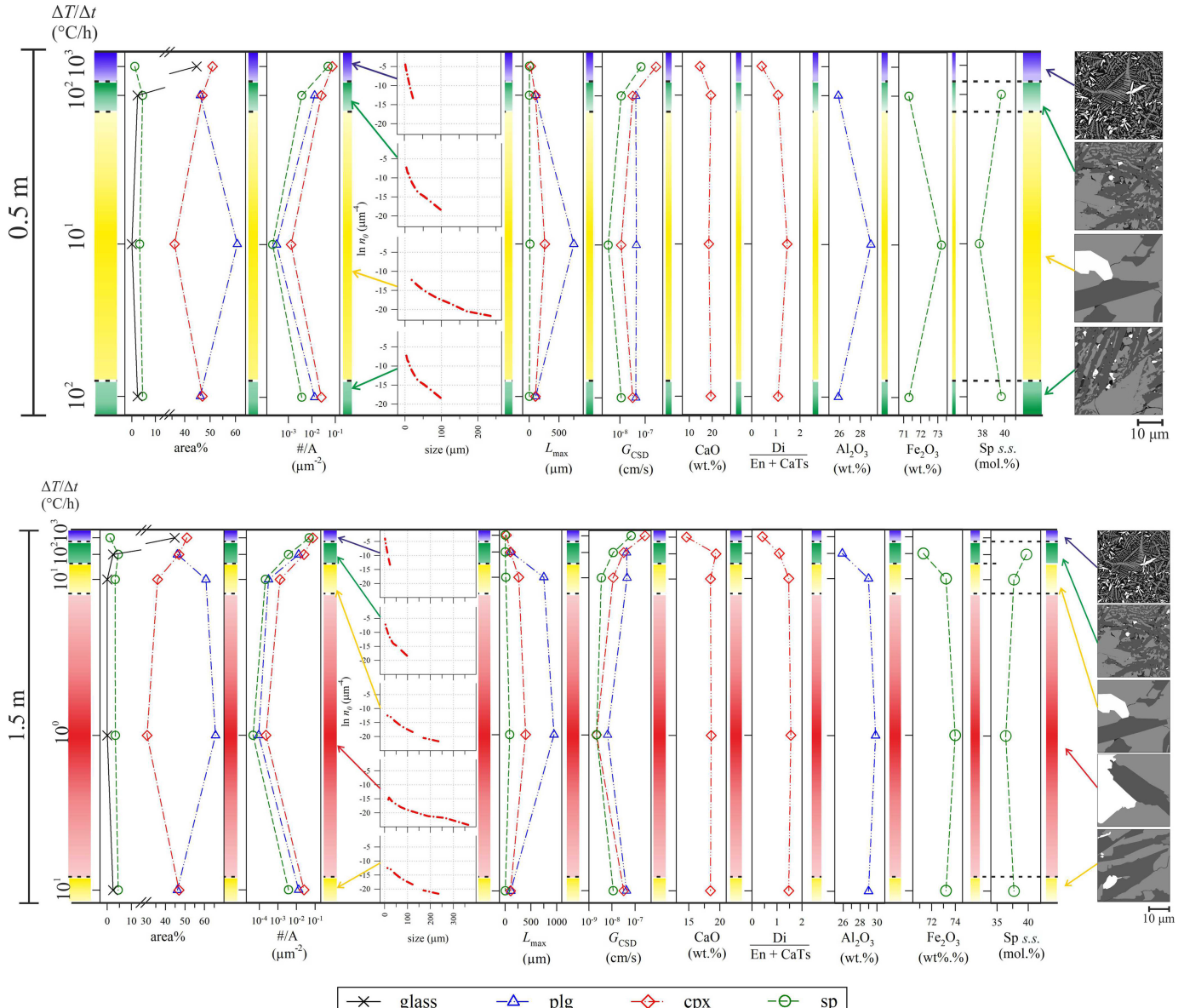
ΔT/Δt (°C/h)
0.5 m
area%
#/A (μm-2)
ln n0 (μm-4)
size (μm)
Lmax (μm)
GCSD (cm/s)
CaO (wt.%)
Di / En + CaTs
Al2O3 (wt.%)
Fe2O3 (wt.%)
Sp s.s. (mol.%)
10 μm
ΔT/Δt (°C/h)
1.5 m
area%
#/A (μm-2)
ln n0 (μm-4)
size (μm)
Lmax (μm)
GCSD (cm/s)
CaO (wt.%)
Di / En + CaTs
Al2O3 (wt.%)
Fe2O3 (wt.%%)
Sp s.s. (mol.%)
10 μm
glass
plg
cpx
sp

Figure 7